01 Jun 2022

Silverrush. Xii. Intensity Mapping for Ly **A** Emission Extending over 100-1000 Comoving Kpc Around Z ∼2-7 Laes with Subaru Hsc-Ssp and Chorus Data

Shotaro Kikuchihara

Yuichi Harikane

Masami Ouchi

Yoshiaki Ono

et. al. For a complete list of authors, see https://scholarsmine.mst.edu/phys_facwork/2243

Recommended Citation

S. Kikuchihara and Y. Harikane and M. Ouchi and Y. Ono and T. Shibuya and R. Itoh and R. Kakuma and A. K. Inoue and H. Kusakabe and K. Shimasaku and R. Momose and Y. Sugahara and S. Kikuta and S. Saito, "Silverrush. Xii. Intensity Mapping for Ly A Emission Extending over 100-1000 Comoving Kpc Around Z ∼2-7 Laes with Subaru Hsc-Ssp and Chorus Data," *Astrophysical Journal*, vol. 931, no. 2, article no. 97, American Astronomical Society; IOP Publishing, Jun 2022.
The definitive version is available at https://doi.org/10.3847/1538-4357/ac69de

The Astrophysical Journal, 931:97 (17pp), 2022 June 1 https://doi.org/10.3847/1538-4357/ac69de

SILVERRUSH. XII. Intensity Mapping for Lyα Emission Extending over 100–1000 Comoving Kpc around $z\sim2-7$ LAEs with Subaru HSC-SSP and CHORUS Data

Shotaro Kikuchihara[1,2], Yuichi Harikane[1,3], Masami Ouchi[1,4,5,6], Yoshiaki Ono[1], Takatoshi Shibuya[7], Ryohei Itoh[1,8], Ryota Kakuma[1,2], Akio K. Inoue[9,10], Haruka Kusakabe[11], Kazuhiro Shimasaku[2,12], Rieko Momose[13,2], Yuma Sugahara[4,9], Satoshi Kikuta[14], Shun Saito[15,6], Nobunari Kashikawa[2,12], Haibin Zhang[16], and Chien-Hsiu Lee[17]

[1] Institute for Cosmic Ray Research, The University of Tokyo, 5-1-5 Kashiwanoha, Kashiwa, Chiba 277-8582, Japan; skiku@icrr.u-tokyo.ac.jp
[2] Department of Astronomy, Graduate School of Science, The University of Tokyo, 7-3-1 Hongo, Bunkyo-ku, Tokyo 113-0033, Japan
[3] Department of Physics and Astronomy, University College London, Gower Street, London WC1E 6BT, UK
[4] National Astronomical Observatory of Japan, 2-21-1 Osawa, Mitaka, Tokyo 181-8588, Japan
[5] Graduate University for Advanced Studies (SOKENDAI), 2-21-1 Osawa, Mitaka, Tokyo 181-8588, Japan
[6] Kavli Institute for the Physics and Mathematics of the Universe (Kavli IPMU, WPI), The University of Tokyo, 5-1-5 Kashiwanoha, Kashiwa, Chiba 277-8583, Japan
[7] Kitami Institute of Technology, 165 Koen-cho, Kitami, Hokkaido 090-8507, Japan
[8] Department of Physics, Graduate School of Science, The University of Tokyo, 7-3-1 Hongo, Bunkyo-ku, Tokyo 113-0033, Japan
[9] Waseda Research Institute for Science and Engineering, Faculty of Science and Engineering, Waseda University, 3-4-1 Okubo, Shinjuku, Tokyo 169-8555, Japan
[10] Department of Physics, School of Advanced Science and Engineering, Faculty of Science and Engineering, Waseda University, 3-4-1 Okubo, Shinjuku, Tokyo 169-8555, Japan
[11] Observatoire de Genève, Université de Genève, 51 chemin de Pégase, 1290 Versoix, Switzerland
[12] Research Center for the Early Universe, Graduate School of Science, The University of Tokyo, 7-3-1 Hongo, Bunkyo-ku, Tokyo 113-0033, Japan
[13] Carnegie Observatories, 813 Santa Barbara Street, Pasadena, CA 91101, USA
[14] Center for Computational Sciences, University of Tsukuba, Ten-nodai, 1-1-1 Tsukuba, Ibaraki 305-8577, Japan
[15] Institute for Multi-messenger Astrophysics and Cosmology, Department of Physics, Missouri University of Science and Technology, 1315 North Pine Street, Rolla, MO 65409, USA
[16] Department of Astronomy, Tsinghua University, No. 1 Qinghuayuan, Beijing 100084, People's Republic of China
[17] W. M. Keck Observatory, Kamuela, HI 96743, USA

Received 2021 August 20; revised 2022 April 21; accepted 2022 April 22; published 2022 May 27

Abstract

We conduct intensity mapping to probe for extended diffuse Lyα emission around Lyα emitters (LAEs) at $z\sim2-7$, exploiting very deep ($\sim$26 mag at 5σ) and large-area ($\sim$4.5 deg^2) Subaru/Hyper Suprime-Cam narrowband (NB) images and large LAE catalogs consisting of a total of 1540 LAEs at $z=2.2$, 3.3, 5.7, and 6.6 obtained by the HSC-SSP and CHORUS projects. We calculate the spatial correlations of these LAEs with $\sim$1–2 billion pixel flux values of the NB images, deriving the average Lyα surface brightness ($SB_{Ly\alpha}$) radial profiles around the LAEs. By carefully estimating systematics such as fluctuations of sky background and point-spread functions, we detect Lyα emission at 100–1000 comoving kpc around $z=3.3$ and 5.7 LAEs at the 3.2σ and 3.7σ levels, respectively, and tentatively (=2.0σ) at $z=6.6$. The emission is as diffuse as $\sim10^{-20}$–10^{-19} erg s^{-1} cm^{-2} arcsec^{-2} and extended beyond the virial radius of a dark matter halo with a mass of 10^{11} $M_\odot$. While the observed $SB_{Ly\alpha}$ profiles have similar amplitudes at $z=2.2$–6.6 within the uncertainties, the intrinsic $SB_{Ly\alpha}$ profiles (corrected for the cosmological dimming effect) increase toward high redshifts. This trend may be explained by increasing hydrogen gas density due to the evolution of the cosmic volume. Comparisons with theoretical models suggest that extended Lyα emission around an LAE is powered by resonantly scattered Lyα photons in the CGM and IGM that originate from the inner part of the LAE and/or neighboring galaxies around the LAE.

Unified Astronomy Thesaurus concepts: Galaxy formation (595); Galaxy evolution (594); High-redshift galaxies (734); Circumgalactic medium (1879); Intergalactic medium (813)

1. Introduction

The gas surrounding a galaxy, called the circumgalactic medium (CGM), falls into the galaxy, triggers star formation activity, and is subsequently ejected from the galaxy due to outflows (e.g., Tumlinson et al. 2017; Péroux & Howk 2020). The hydrogen gas inside the CGM can be traced by Lyα emission, which is observed as a Lyα halo (LAH). Therefore, observing LAHs is key to understanding the properties and kinematics of the CGM and eventually providing information on galaxy formation and evolution.

Many studies have detected LAHs around nearby galaxies (e.g., Östlin et al. 2009; Hayes et al. 2013, 2014). At high redshift ($z>2$), meanwhile, LAHs have been identified mainly around massive galaxies, such as Lyman break galaxies (e.g., Hayashino et al. 2004; Swinbank et al. 2007; Steidel et al. 2011) and quasars (e.g., Goto et al. 2009; Cantalupo et al. 2014; Martin et al. 2014; Borisova et al. 2016; Arrigoni Battaia et al. 2019; Kikuta et al. 2019; Mukae et al. 2020; Zhang et al. 2020). However, it remains difficult to detect diffuse emission around less massive star-forming galaxies, such as Lyα emitters (LAEs), at high redshift due to their faintness and sensitivity limits.

To overcome this difficulty, Rauch et al. (2008), for example, performed a very deep (92 hr) long-slit observation with the ESO Very Large Telescope (VLT) FOcal Reducer and low dispersion Spectrograph 2 that reached a 1σ surface brightness (SB) detection

limit of 8×10^{-20} erg cm^{-2} s^{-1} arcsec^{-2}. They investigated 27 LAEs at $z=2.67$–3.75, identifying Lyα emission extending over 26 physical kpc (pkpc) around one of the LAEs. Individual detections of many high-redshift LAHs have been enabled by the advent of the Multi-Unit Spectroscopic Explorer (MUSE) installed on the VLT. Recently, Leclercq et al. (2017) identified individual LAHs around 145 LAEs at $z=3$–6 in the Hubble Ultra Deep Field with the VLT/MUSE (see also Wisotzki et al. 2016). Their data reached an SB limit of $\lesssim10^{-19}$ erg s^{-1} cm^{-2} arcsec^{-2} at radii of >10 pkpc.

A stacking method has been widely used to obtain averaged radial profiles of Lyα emission with high signal-to-noise ratios (S/Ns; e.g., Matsuda et al. 2012; Momose et al. 2014, 2016; Xue et al. 2017; Wisotzki et al. 2018; Wu et al. 2020). For example, Momose et al. (2014) stacked Subaru Telescope/Suprime-Cam (SC) narrowband (NB) images around >100 LAEs at $z=2.2$–6.6, obtaining Lyα radial profiles to ~50 pkpc radial scales. Matsuda et al. (2012) and Momose et al. (2016) investigated the LAH size dependence on LAE properties, such as Lyα luminosity, rest-frame ultraviolet (UV) magnitude, and overdensity, at $z=3.1$ and 2.2, respectively. We note that some studies (e.g., Bond et al. 2010; Feldmeier et al. 2013; Jiang et al. 2013) reported no evidence of extended Lyα emission at $z>2$.

Another approach is the intensity mapping technique (see Kovetz et al. 2017 for a review; see also Carilli 2011; Gong et al. 2011; Silva et al. 2013; Pullen et al. 2014; Comaschi & Ferrara 2016a, 2016b; Li et al. 2016; Fonseca et al. 2017), which utilizes cross-correlation functions between objects and their emission or absorption spectra. This technique enables us to detect signals from targeted galaxies with a high S/N by efficiently estimating and removing contaminating signals from foreground interlopers. Croft et al. (2016, 2018) derived cross-correlation functions between the Lyα emission and quasar positions at $z=2$–3.5 using data from the Sloan Digital Sky Survey (SDSS; Eisenstein et al. 2011) Baryon Oscillation Spectroscopic Survey (Dawson et al. 2013). This work enabled the detection of positive signals over the $>10^3$ pkpc radial scale.

Recently, Kakuma et al. (2021) applied the intensity mapping technique to LAEs at $z=5.7$ and 6.6 using Subaru/Hyper Suprime-Cam (HSC) data. They tentatively identified very diffuse ($\sim10^{-20}$ erg s^{-1} cm^{-2} arcsec^{-2}) Lyα emission that, surprisingly, is extended over the virial radius ($R_{\rm vir}$) of a dark matter halo (DMH). Their finding has shed light on the potential existence of Lyα-emitting hydrogen gas much beyond $R_{\rm vir}$ around LAEs in the reionization epoch.

Such extended Lyα emission has also recently been identified at lower redshifts. Umehata et al. (2019) observed Lyα emission from the SSA 22 protocluster field at $z=3.1$ with MUSE, finding filamentary structure extended over $\sim10^3$ pkpc. Bacon et al. (2021) also identified similarly extended Lyα emission around the $z\sim3-4$ LAEs in the overdense regions in the MUSE Extremely Deep Field. While these discoveries in themselves are impressive, they focus on individual LAEs residing in overdense regions. This motivates us to investigate whether even field LAEs at low redshifts ubiquitously harbor such extended Lyα emission.

In this paper, we exploit NB images offered in two Subaru/HSC surveys, the Cosmic HydrOgen Reionization Unveiled with Subaru (CHORUS; Inoue et al. 2020) and the Subaru Strategic Program (HSC-SSP; Aihara et al. 2019), which enable us to trace Lyα emission from LAEs across $z=2.2$–6.6. We aim to systematically investigate diffuse Lyα emission extended beyond $R_{\rm vir}$ around $z=2.2$–6.6 LAEs, taking advantage of the intensity mapping technique and ultradeep images of the CHORUS and HSC-SSP projects. In addition, we use the LAE catalog constructed by Ono et al. (2021) as a part of the Systematic Identification of LAEs for Visible Exploration and Reionization Research Using Subaru HSC (SILVERRUSH) project (Ouchi et al. 2018). Covering a very wide area (>1 deg^2), this catalog helps us to study Lyα emission with a large number of LAEs in general fields.

Another open question about extended Lyα emission is its physical origin (see the review by Ouchi et al. 2020 and Figure 15 of Momose et al. 2016). Theoretical studies have suggested several physical processes, which can be classified mainly into (1) resonant scattering and (2) in situ production. In resonant scattering, Lyα photons are produced in the interstellar medium (ISM) of the galaxy and then resonantly scattered by neutral hydrogen gas while escaping the galaxy into the CGM and intergalactic medium (IGM; e.g., Laursen & Sommer-Larsen 2007; Laursen et al. 2011; Steidel et al. 2011; Zheng et al. 2011; Dijkstra & Kramer 2012; Jeeson-Daniel et al. 2012; Verhamme et al. 2012; Kakiichi & Dijkstra 2018; Smith et al. 2018, 2019; Garel et al. 2021). For in situ production, Lyα photons are produced not inside the galaxy but in the CGM. This can be further classified into three processes: (i) recombination, (ii) collisional excitation, and (iii) star formation. In recombination, ionizing radiation from the galaxy or extragalactic background (UVB) photoionizes the hydrogen gas in the CGM, which in turn emits Lyα emission via recombination ("fluorescence"; e.g., Cantalupo et al. 2005; Furlanetto et al. 2005; Kollmeier et al. 2010; Lake et al. 2015; Mas-Ribas & Dijkstra 2016; Gallego et al. 2018; Mas-Ribas et al. 2017b). Collisional excitation: hydrogen gas in the CGM is compressively heated by shocks and then emits Lyα photons by converting its gravitational energy into Lyα emission while accreting onto the galaxy ("gravitational cooling" or "cold stream"; e.g., Haiman et al. 2000; Fardal et al. 2001; Goerdt et al. 2010; Faucher-Giguère et al. 2010; Rosdahl & Blaizot 2012; Lake et al. 2015). In star formation, Lyα emission is produced by star formation in unresolved dwarfs surrounding the galaxy ("satellite galaxies"; e.g., Mas-Ribas et al. 2017a, 2017b).

To explain the Lyα emission extended larger than $R_{\rm vir}$, Kakuma et al. (2021) compared the observed Lyα SB profiles against the prediction by Zheng et al. (2011) that considers resonant scattering, but large uncertainties of the data prevented drawing a conclusion. Bacon et al. (2021) suggested that such extended Lyα emission originates from a large population of unresolved and ultrafaint ($<10^{40}$ erg s^{-1}) dwarfs clustering around the LAEs. In the case of Umehata et al. (2019), extended Lyα emission is attributed to the ionizing radiation caused by intense star formation or active galactic nuclei. Since their comparisons are limited to specific cases for each individual LAE at each redshift, we still need to comprehensively investigate the key origin(s) by utilizing multiple models at multiple redshifts.

This paper is organized as follows. Our data are described in Section 2. In Section 3, we use the intensity mapping technique to derive the cross-correlation SB of Lyα emission around the LAEs. We discuss the redshift evolution and physical origins of extended Lyα emission in Section 4 and summarize our findings in Section 5.

Throughout this paper, magnitudes are given in the AB system (Oke & Gunn 1983). We adopt the concordance cosmology with $\Omega_{m,0}=0.7$, $\Omega_{\Lambda,0}=0.3$, and $H_0=70$ km s^{-1} Mpc^{-1}, where $1''$ corresponds to transverse sizes of (8.3, 7.5, 5.9, 5.4) pkpc and (26, 32, 39, 41) comoving kpc (ckpc) at $z=$ (2.2, 3.3, 5.7, 6.6).

2. Data

In this section, we describe the images and sample catalogs used for our analyses. All of the images and catalogs are based on Subaru/HSC data.

2.1. Images

We use NB and broadband (BB) imaging data that were obtained in two Subaru/HSC surveys, HSC-SSP and CHORUS. The HSC-SSP and CHORUS data were obtained in 2014 March–2018 January and 2017 January–2018 December, respectively. We specifically use the internal data of the S18A release. The HSC-SSP survey is a combination of three layers: Wide, Deep, and UltraDeep (UD). We use the UD layer images in the fields of the Cosmological Evolution Survey (UD-COSMOS; Scoville et al. 2007) and Subaru/XMM Deep Survey (UD-SXDS; Sekiguchi et al. 2005) because the wide survey areas ($\sim$2 deg^2 for each field) and deep imaging (the 5σ limiting magnitudes are $\sim$26 mag in a $2''$ diameter aperture) in these fields are advantageous for the detection of very diffuse Lyα emission. The CHORUS data were obtained over the UD-COSMOS field. The HSC-SSP and CHORUS data were reduced with the HSC pipeline v6.7 (Bosch et al. 2018).

The HSC-SSP provides the data of two NB (NB816 and NB921) filters in the UD-COSMOS and UD-SXDS fields, while the CHORUS images are offered in four NB (NB387, NB527, NB718, and NB973) filters in the UD-COSMOS field. In this work, we present the results in the NB387, NB527, NB816, and NB921 filters. The NB718 and NB973 filters are not used in the following sections because the number of LAEs and the image depths are not sufficient to detect diffuse Lyα emission. The NB387, NB527, NB816, and NB921 filters are centered at 3863, 5260, 8177, and 9215 Å with the full widths at half maximum (FWHMs) of 55, 79, 113, and 135 Å, respectively, which cover the observed wavelengths of Lyα emission from $z=2.178\pm0.023$, 3.327 ± 0.032, 5.726 ± 0.046, and 6.580 ± 0.056, respectively. Five BB (g-, $r2$-, $i2$-, z-, and y-band) filters are also available in both HSC-SSP and CHORUS. Figure 1 shows the NB and BB filter throughputs, and Table 1 summarizes the images and filters.

Bright sources in the NB and BB images must be masked, since they contaminate diffuse emission. We thus mask pixels flagged with either `DETECT` or `BRIGHT_OBJECT` using the masks provided by the HSC pipeline (termed *original* masks). A pixel is flagged with `DETECT` or `BRIGHT_OBJECT` when the pixel is covered by a detected ($\geqslant5\sigma$) object or affected by nearby bright sources, respectively. However, because some bright sources are missed in the original masks due to bad photometry, the HSC-SSP team offered new masks that mitigated this problem (hereafter termed *revised* masks).[18] The revised mask is defined based on the bright stars cataloged in the Gaia Data Release 2 (Gaia Collaboration et al. 2018). We find that the stars brighter than $\sim$18 mag are masked. We adopt the revised masks in addition to the original masks to flag `BRIGHT_OBJECT`. We use the revised g-, $r2$-, z-, and y-band masks for the NB387, NB527, NB816, and NB921 images, respectively, because the revised masks are offered only in the BB filters. For the BB images, we use the revised masks defined for each BB filter. We visually confirm that these criteria successfully cover bright sources and contaminants in the images.

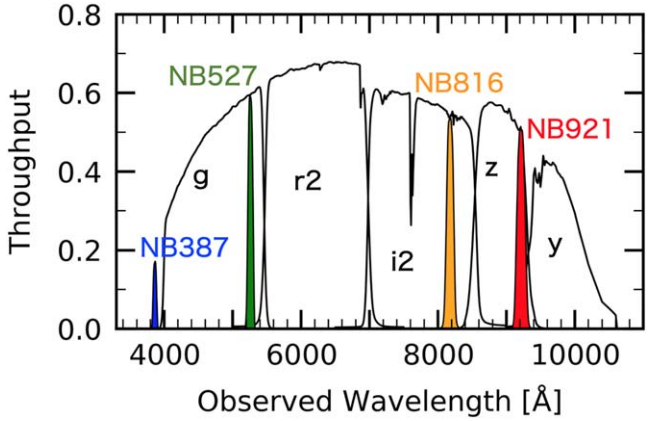

Figure 1. Effective response curves of the HSC NB filters NB387 (blue), NB527 (green), NB816 (orange), and NB921 (red) and BB filters g, $r2$, $i2$, z, and y (black). These response curves include the quantum efficiency of the HSC CCD, the transmittance of the dewar window of the primary focus unit, the reflectivity of the primary mirror, and the airmass at the telescope site.

2.2. LAE Sample

We use the LAE catalog of Ono et al. (2021). They selected LAE candidates based on color and removed contaminants by a convolutional neural network (CNN) and visual inspection. Their final catalog includes (542, 959, 395, 150) LAEs at $z=$ (2.2, 3.3, 5.7, 6.6) in the UD-COSMOS field and (560, 75) LAEs at $z=$ (5.7, 6.6) in the UD-SXDS field.

The NB images of the UD-COSMOS and UD-SXDS fields are deepest at the center and become shallower toward the edges (Hayashi et al. 2020; Inoue et al. 2020). We thus exclude LAEs outside of the boundaries shown with the black dashed circles in Figures 2 and 3. The boundaries are defined such that the limiting magnitudes outside are shallower than those at the center by $\sim$0.2 mag.

We estimate the Lyα line luminosities ($L_{\mathrm{Ly}\alpha}$) following Shibuya et al. (2018; see also Itoh et al. 2018). First, we measure the NB (BB) magnitudes m_{NB} (m_{BB}) of the LAEs at $z=2.2$, 3.3, 5.7, and 6.6 in the NB387 (g-band), NB527 ($r2$-band), NB816 (z-band), and NB921 (y-band) filters, respectively. The magnitudes are measured with a $2''$ diameter aperture because it efficiently covers the point-spread function (PSF), whose FWHM is $0\farcs8$–$1\farcs1$ (Ono et al. 2021). The NB387 magnitudes are corrected for the systematic zero-point offset by 0.45 mag, following the recommendation by the HSC-SSP team.[19] Next, we follow Shibuya et al. (2018) to derive the Lyα line fluxes ($f_{\mathrm{Ly}\alpha}$) from m_{NB} and m_{BB}, assuming a flat UV continuum and the IGM attenuation model of Inoue et al. (2014). Lastly, the values of $L_{\mathrm{Ly}\alpha}$ are derived via

[18] https://hsc-release.mtk.nao.ac.jp/doc/index.php/bright-star-masks-2/

[19] https://hsc-release.mtk.nao.ac.jp/doc/index.php/known-problems-2/#hsc-link-10

Table 1
Summary of the NB Filters and Images

NB	λ_c (Å)	FWHM (Å)	z_{LAE}	UD-COSMOS Area (deg^2)	UD-COSMOS $m_{NB,5\sigma}$ (mag)	UD-SXDS Area (deg^2)	UD-SXDS $m_{NB,5\sigma}$ (mag)
(1)	(2)	(3)	(4)	(5)	(6)	(7)	(8)
NB387 (CHORUS)	3863	55	2.178 ± 0.023	1.561	25.67	⋯	⋯
NB527 (CHORUS)	5260	79	3.327 ± 0.032	1.613	26.39	⋯	⋯
NB816 (HSC-SSP)	8177	113	5.726 ± 0.046	2.261	25.75	2.278	25.61
NB921 (HSC-SSP)	9215	135	6.580 ± 0.056	2.278	25.48	2.278	25.31

Note. Columns: (1) NB filter. (2) and (3) Central wavelength (λ_c) and FWHM of the NB filter transmission curve. (4) Redshift range of the LAEs whose Lyα emission enters the NB filter. (5) and (6) Effective area and 5σ limiting NB magnitude ($m_{NB,5\sigma}$) in the UD-COSMOS field. The $m_{NB,5\sigma}$ value is measured with a 2″ diameter aperture in each patch and then averaged over the field. See Inoue et al. (2020) and Hayashi et al. (2020) for the spatial variance of $m_{NB,5\sigma}$. The $m_{NB,5\sigma}$ value in NB387 is corrected for the systematic zero-point offset by 0.45 mag (see Section 2.2). (7) and (8) Same as columns (5) and (6) but for the UD-SXDS field. The values in this table are cited from Ono et al. (2021).

$L_{Ly\alpha} = 4\pi d_L(z_{LAE})^2 f_{Ly\alpha}$, where $d_L(z_{LAE})$ denotes the luminosity distance to the LAE at redshift z_{LAE}.

Although the completeness of the LAEs is as high as $\gtrsim$90% at $m_{NB} \lesssim 24.5$ in the CNN of Ono et al. (2021), faint LAEs may be missed in the observations and selection. To ensure completeness, we use only LAEs whose $L_{Ly\alpha}$ values are larger than the modes (peaks) of the $L_{Ly\alpha}$ histograms, which are represented as $L_{Ly\alpha}^{min}$ in Table 2. This sample, termed the *all* sample, consists of (289, 762, 210, 56) LAEs at $z = (2.2, 3.3, 5.7, 6.6)$ and (199, 24) LAEs at $z = (5.7, 6.6)$ in the UD-COSMOS and UD-SXDS fields, respectively. To accurately compare the LAEs of different redshifts at similar $L_{Ly\alpha}$ values, we further exclude faint LAEs from the *all* sample such that the mean $L_{Ly\alpha}$ values are equal to $10^{42.9}$ erg s^{-1} at each redshift. This selection results in (37, 123, 125) LAEs at $z = (2.2, 3.3, 5.7)$ and 88 LAEs at $z = 5.7$ in the UD-COSMOS and UD-SXDS fields, respectively, which we hereafter refer to as the *bright* subsample. At $z = 6.6$, since the mean $L_{Ly\alpha}$ values of the *all* sample are $10^{43.0}$ erg s^{-1} in both the UD-COSMOS and UD-SXDS fields, we also use the *all* sample as the *bright* subsample. In summary, we use a total of 1540 and 453 LAEs in the UD-COSMOS+UD-SXDS fields as the *all* sample and the *bright* subsample, respectively. The $L_{Ly\alpha}$ values and sample sizes are summarized in Table 2. The sky distributions of the LAEs in the UD-COSMOS and UD-SXDS fields are presented in Figures 2 and 3, respectively.

A major update of our data compared to Kakuma et al. (2021) is that we add 1051 new LAEs at $z = 2.2$ and 3.3 using the CHORUS data. The catalog of $z = 5.7$ and 6.6 LAEs is also updated in that we use the latest catalog constructed by Ono et al. (2021) based on HSC-SSP S18A images, while Kakuma et al. (2021) used the S16A catalog taken from Shibuya et al. (2018). The number of LAEs of Ono et al. (2021; a total of 1180 for the UD-COSMOS and UD-SXDS fields) increases from that of Kakuma et al. (2021; a total of 630) because the limiting magnitudes are improved by ∼0.5 mag. However, we exclude the LAEs that are faint or close to the field boundaries from the sample of Ono et al. (2021), which results in the number of LAEs (=489) and the minimum NB magnitudes (∼25–25.5 mag) comparable to those of Kakuma et al. (2021). We use the same images as Kakuma et al. (2021; i.e., those taken from the HSC-SSP S18A release) in NB816 and NB921, while our masking prescription may be slightly different.

2.3. NonLAE Sample

Although the intensity mapping technique can remove spurious signals from low-redshift interlopers, other systematics, such as the sky background and PSF, may still contaminate LAE signals. To estimate the contribution from these systematics, we use foreground sources, which we hereafter term "NonLAEs." Because NonLAEs should correlate only with the systematics, but not with Lyα emission from LAEs, we estimate these systematics by applying the intensity mapping technique to NonLAEs.

We construct NonLAE samples as follows. First, we detect sources in the NB images using `SExtractor` (Bertin & Arnouts 1996). Second, we select only sources that are sufficiently bright ($\lesssim$26 mag) in the *g*, *r*2, and *i*2 bands to remove spurious sources and artifacts. Third, we randomly select the sources such that they have the same sky, FWHM–magnitude distributions in NB (FWHM$_{NB}$–m_{NB}) as those of the LAEs in each field at each redshift. In this way, $\sim 10^3$ sources are selected, which we define as NonLAEs. We present the FWHM$_{NB}$–m_{NB} distributions of the LAEs and corresponding NonLAEs in Figures 4 and 5.

To test whether our NonLAE selection biases the measurement of the systematics, we first estimate the fraction of low-redshift line emitters that mimic Lyα emission (for example, the Hα line emitted from a galaxy at $z = 0.237$–0.254 contaminates the Lyα flux measured with the NB816 image). Based on the colors of low-redshift line emitters given by Hayashi et al. (2020), we find that the fraction of low-redshift line emitters included in the NonLAEs is no more than ∼5%. Second, we estimate the redshifts of the NonLAEs by cross-matching them with the MIZUKI photometric redshift catalog (Tanaka 2015) and the SDSS spectroscopic source catalog (Blanton et al. 2017). As a result, only up to ∼3% of the cross-matched NonLAEs are at the redshifts that might contaminate the Lyα flux (for example, $z = 0.237$–0.254 for the NB816 case). These results suggest that such low-line emitters have only a negligible impact on the measurement of the systematics. Indeed, the measurement remains unchanged within the 1σ uncertainties even when we exclude such potential line emitters from the NonLAE sample. Furthermore, we also confirm that using blank locations as the NonLAEs produces the measurement consistent with the above within the 1σ uncertainties at $\gtrsim$100 ckpc. To summarize these results, our NonLAE selection is very unlikely to bias the measurement of the systematics.

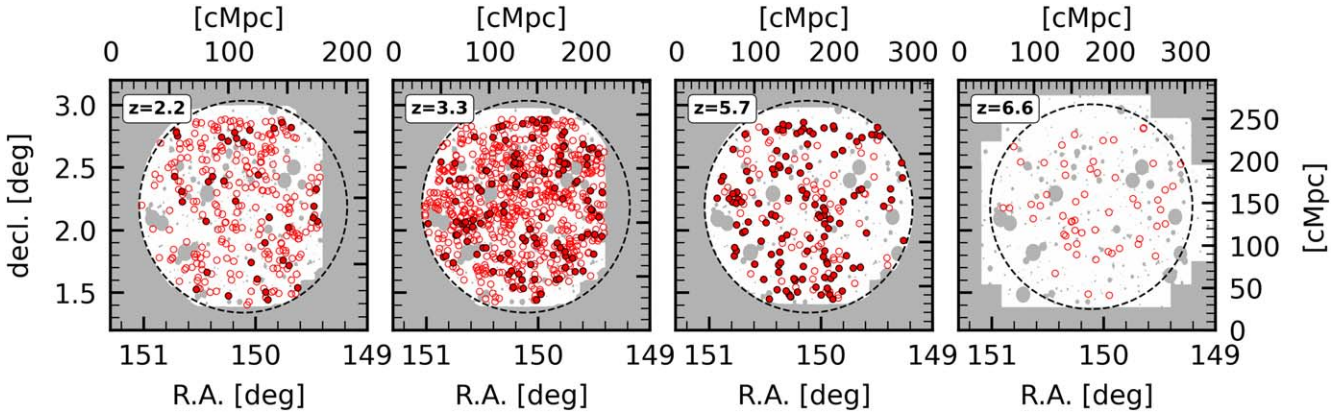

Figure 2. Sky distributions of the LAEs in the UD-COSMOS field at $z = 2.2$, 3.3, 5.7, and 6.6, from left to right. The open red circles show the positions of the LAEs included in the *all* sample but not the *bright* subsample, while the filled red circles indicate the positions of the *bright* subsample LAEs (i.e., *all* sample LAEs are represented by the open+filled red circles). We use the LAEs inside the black dashed circles. The background white shaded area shows the NB387, NB527, NB816, and NB921 images, from left to right. The gray shaded area shows the regions where the pixel is masked or a UD image is not offered. Note that the distribution of the *bright* subsample at $z = 6.6$ is not displayed because we also treat the *all* sample also as the *bright* subsample at $z = 6.6$.

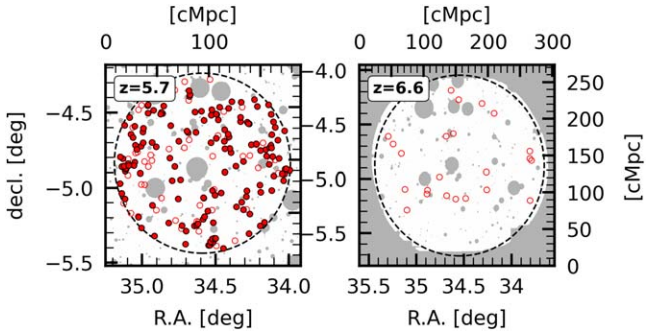

Figure 3. Same as Figure 2 but for the UD-SXDS field at $z = 5.7$ (left) and 6.6 (right).

3. Intensity Mapping Analysis

In this section, we derive the SB radial profiles of Lyα emission around the LAEs using the intensity mapping technique.

3.1. Cross-correlation Functions

We compute SB as a cross-correlation function between intensities of emission in a given band (XB) and given objects (OBJs), $\mathrm{SB}_{\mathrm{XB}\times\mathrm{OBJ}}$,[20] via

$$\mathrm{SB}_{\mathrm{XB}\times\mathrm{OBJ},\nu}(r) = \frac{1}{N_{r,\mathrm{OBJ}}} \sum_{i=1}^{N_{r,\mathrm{OBJ}}} \mu_{\nu,i}^{(\mathrm{XB})} \quad (1)$$

and

$$\mathrm{SB}_{\mathrm{XB}\times\mathrm{OBJ}}(r) = \mathrm{SB}_{\mathrm{XB}\times\mathrm{OBJ},\nu}(r) \times \mathrm{FWHM}_{\mathrm{XB}}. \quad (2)$$

The pixel of the ith pixel–OBJ pair has a pixel value of $\mu_{\nu,i}^{(\mathrm{XB})}$ in the XB image in units of erg s^{-1} cm^{-2} Hz^{-1} arcsec^{-2}. In NB387, we multiply $\mu_{\nu,i}^{(\mathrm{NB387})}$ by 1.5 to correct for the zero-point offset of 0.45 mag (see Section 2.2). The summation runs over the $N_{r,\mathrm{OBJ}}$ pixel–OBJ pairs that are separated by a spatial distance r. We use pixels at distances of between 1.″5 and 40″ from each OBJ (corresponding to the outer part of the CGM and outside), which are then divided into six radial bins. A total of $\sim(1\text{–}2)\times10^9$ pixels are used for the calculation at each redshift. Here $\mathrm{FWHM}_{\mathrm{XB}}$ represents the XB filter width (in units of Hz) corrected for IGM attenuation, derived via

$$\mathrm{FWHM}_{\mathrm{XB}} = \frac{\int_0^\infty e^{-\tau_{\mathrm{eff}}(\nu)} T_{\mathrm{XB}}(\nu) d\nu / \nu}{T_{\mathrm{XB}}(\nu_\alpha)/\nu_\alpha}, \quad (3)$$

where $T_{\mathrm{XB}}(\nu)$ denotes the transmittance of the XB filter, and ν_α is the observed Lyα line frequency. We adopt the IGM optical depth $\tau_{\mathrm{eff}}(\nu)$ from Inoue et al. (2014).

The statistical uncertainty of $\mathrm{SB}_{\mathrm{XB}\times\mathrm{OBJ}}$ is estimated by the bootstrap method. We randomly resample objects while keeping the sample size and calculated $\mathrm{SB}_{\mathrm{XB}\times\mathrm{OBJ}}$. We then repeat the resampling 10^4 times, adopting the 1σ standard deviation of the $\mathrm{SB}_{\mathrm{XB}\times\mathrm{OBJ}}$ values as the 1σ statistical uncertainty of the original $\mathrm{SB}_{\mathrm{XB}\times\mathrm{OBJ}}$. At $z = 2.2$ and 3.3, the UD-SXDS field is not observed in CHORUS, which prevents the estimation of the field variance between the UD-COSMOS and UD-SXDS fields. Therefore, we alternatively divide the LAEs at $z = 3.3$ into four equal regions and derive $\mathrm{SB}_{\mathrm{NB}\times\mathrm{LAE}}$ in each region. We find that the deviation of $\mathrm{SB}_{\mathrm{NB}\times\mathrm{LAE}}$ among the four regions is $\sim$10%–20% of the averaged values. We add this deviation in quadrature to the statistical uncertainties of $\mathrm{SB}_{\mathrm{NB}\times\mathrm{LAE}}$.

3.2. Lyα SB

We estimate the SB of Lyα emission ($\mathrm{SB}_{\mathrm{Ly}\alpha}$) around the LAEs as follows. First, we subtract the systematics ($\mathrm{SB}_{\mathrm{NB}\times\mathrm{NonLAE}}$) from the emission from the LAEs ($\mathrm{SB}_{\mathrm{NB}\times\mathrm{LAE}}$) via

$$\mathrm{SB}_{\mathrm{NB}} = \mathrm{SB}_{\mathrm{NB}\times\mathrm{LAE}} - \mathrm{SB}_{\mathrm{NB}\times\mathrm{NonLAE}}. \quad (4)$$

Uncertainties in $\mathrm{SB}_{\mathrm{NB}}$ propagate from those of $\mathrm{SB}_{\mathrm{NB}\times\mathrm{LAE}}$ and $\mathrm{SB}_{\mathrm{NB}\times\mathrm{NonLAE}}$. We present the radial profiles of the $\mathrm{SB}_{\mathrm{NB}\times\mathrm{LAE}}$, $\mathrm{SB}_{\mathrm{NB}\times\mathrm{NonLAE}}$, and $\mathrm{SB}_{\mathrm{NB}}$ of the *all* sample and *bright* subsample in Figures 6 and 7, respectively.

We use Fisher's method (Fisher & Aylmer 1970) to estimate the S/Ns of $\mathrm{SB}_{\mathrm{NB}}$ over all of the radial bins, following Kakuma et al. (2021). Generally, a p-value is expressed as

$$p = \int_{\mathrm{S/N}}^\infty \mathcal{N}(x;\, \mu = 0,\, \sigma = 1) dx, \quad (5)$$

[20] The right-hand side of Equation (1) represents a cross-correlation function, which has usually been referred to as ξ in previous work (e.g., Croft et al. 2016, 2018; Bielby et al. 2017; Momose et al. 2021a, 2021b). However, we refer to this function as "SB," since the cross-correlation function is equivalent to surface brightness in our analyses.

Table 2
Summary of the Sample

	UD-COSMOS			UD-SXDS			
$z_{\rm LAE}$	$\log L_{\rm Ly\alpha}^{\rm min}$ (erg s^{-1})	$\log L_{\rm Ly\alpha}^{\rm mean}$ (erg s^{-1})	$N_{\rm LAE}$	$\log L_{\rm Ly\alpha}^{\rm min}$ (erg s^{-1})	$\log L_{\rm Ly\alpha}^{\rm mean}$ (erg s^{-1})	$N_{\rm LAE}$	$N_{\rm LAE,total}$
(1)	(2)	(3)	(4)	(5)	(6)	(7)	(8)
All Sample							
2.2	42.2	42.5	289	⋯	⋯	⋯	289
3.3	42.1	42.5	762	⋯	⋯	⋯	762
5.7	42.6	42.8	210	42.2	42.8	199	409
6.6	42.8	43.0	56	42.9	43.0	24	80
$N_{\rm LAE,total}$			1317			223	1540
Bright Subsample							
2.2	42.6	42.9	37	⋯	⋯	⋯	37
3.3	42.6	42.9	123	⋯	⋯	⋯	123
5.7	42.7	42.9	125	42.7	42.9	88	213
6.6[a]	42.8	43.0	56	42.9	43.0	24	80
$N_{\rm LAE,total}$			341			112	453

Notes. Columns: (1) Redshift. (2) and (3) Minimum and mean Lyα luminosity of the *all* sample (top) and *bright* subsample (bottom) in the UD-COSMOS field, measured with a 2″ diameter aperture. (4) Number of LAEs. The total number of LAEs over $z = 2.2$–6.6 is shown in the bottom row. (5)–(7) Same as columns (2)–(4) but for the UD-SXDS field. (8) Total number of LAEs at each z.
[a] At $z = 6.6$, we also treat the *all* sample as the *bright* subsample in each field (see Section 2.2).

where $\mathcal{N}(x;\ \mu = 0,\ \sigma = 1)$ is a Gaussian distribution with an expected value $\mu = 0$ and a variance $\sigma^2 = 1$. We thus use this equation to convert the S/N in the ith radial bin (S/N_i) into the p-value in that bin ($_{pi}$). The χ^2 value over all of the radial bins ($1 \leqslant i \leqslant N$), $\hat{\chi}^2$, is then calculated as $\hat{\chi}^2 = -2\sum_{i=1}^{N} \ln(p_i)$. Since $\hat{\chi}^2$ follows a χ^2_{2N} distribution with $2N$ degrees of freedom, $\chi^2(x;\ {\rm dof} = 2N)$, the p-value over all of the radial bins, $\hat{p}$, is derived as

$$\hat{p} = \int_{\hat{\chi}^2}^{\infty} \chi^2(x;\ {\rm dof} = 2N)dx. \quad (6)$$

We convert this to the S/N over all of the radial bins by solving Equation (5) for S/N.

The black vertical dashed lines in Figures 6 and 7 indicate $R_{\rm vir}$. Following the observational results by Ouchi et al. (2010) and Kusakabe et al. (2018), we assume that the DMHs hosting LAEs have halo masses ($M_{\rm halo}$) of $10^{11}\,M_\odot$ at all redshifts, which corresponds to an $R_{\rm vir}$ value of ∼150 ckpc.

For the *all* sample (Figure 6), we unfortunately see no clear ($<1\sigma$) detection at $z = 2.2$. On the contrary, at $z = 3.3$, $SB_{\rm NB}$ is significantly positive over wide scales from $\sim 10^2$ to 10^3 ckpc with S/N = 3.2. At $z = 5.7$, $SB_{\rm NB}$ is significantly positive at ∼80–10^3 ckpc in the UD-COSMOS field with S/N = 4.7, while the signal in the UD-SXDS field is weak (a similar trend is reported in Kakuma et al. 2021). To investigate the averaged signal between the two fields, we mean $SB_{\rm NB}$ in both fields with weights of the inverse of the $SB_{\rm NB}$ uncertainties and add the uncertainties in quadrature. As a result, we identify positive signals with S/N = 3.7. At $z = 6.6$, $SB_{\rm NB}$ is positive at ∼80–200 ckpc in both fields. Averaging $SB_{\rm NB}$ over the two fields, we tentatively identify a positive signal with S/N = 2.0. The values of $SB_{\rm NB}$ at $z = 3.3$–6.6 are as diffuse as $\sim 10^{-20}$–10^{-19} erg s^{-1} cm^{-2} arcsec^{-2}.

For the *bright* subsample (Figure 7), the signals at $z = 2.2$ and 3.3 are not significant. Meanwhile, we find the positive signal with S/N = 2.0 when averaging $SB_{\rm NB}$ over the UD-COSMOS and UD-SXDS fields at $z = 5.7$.

The UV continuum emission might contribute to the $SB_{\rm NB}$ in addition to the Lyα line emission. We thus estimate the SB of the UV continuum emission, $SB_{{\rm cont},\nu}$, using

$$SB_{{\rm cont},\nu} < SB_{{\rm BB},\nu} \equiv SB_{{\rm BB}\times{\rm LAE},\nu} - SB_{{\rm BB}\times{\rm random},\nu}, \quad (7)$$

where $SB_{{\rm BB}\times{\rm LAE},\nu}$ ($SB_{{\rm BB}\times{\rm random},\nu}$) represents the SB value that is derived from the cross-correlation function between the BB images and LAEs (random sources) in units of erg s^{-1} cm^{-2} Hz^{-1} arcsec^{-2}. To estimate the sky background, we use random sources, not NonLAEs, since it is difficult to match the $FWHM_{\rm NB}$–$m_{\rm NB}$ distributions of the NonLAEs with those of the LAEs due to the faintness of the LAEs in the BB. Since $SB_{{\rm BB}\times{\rm random},\nu}$ neglects signals from the PSF, $SB_{{\rm BB},\nu}$ should be treated as the upper limit of $SB_{{\rm cont},\nu}$. As shown in Figure 8 as an example, the values of $SB_{{\rm cont},\nu}$ at $z = 2.2$–6.6 are consistent with null detection within $\sim(1$–$2)\sigma$ uncertainties. Additionally, we confirm that the UV continuum emission contributing to $SB_{\rm NB}$, i.e., $SB_{{\rm cont},\nu} \times FWHM_{\rm NB}$, is negligible compared to $SB_{\rm NB}$. Therefore, we hereafter assume that $SB_{\rm NB}$ is equivalent to the Lyα SB ($SB_{\rm Ly\alpha}$).

In summary, we identify very diffuse ($\sim 10^{-20}$–10^{-19} erg s^{-1} cm^{-2} arcsec^{-2}) Lyα signals beyond $R_{\rm vir}$ around the *all* sample LAEs clearly at $z = 3.3$ and 5.7 with S/N ∼ 3–4 and tentatively at $z = 6.6$ with S/N ∼ 2. These results imply the potential existence of very diffuse and extended Lyα emission around $z = 3.3$–6.6 LAEs. The significant detections at $z = 3.3$ and 5.7 are presumably due to the large number of LAEs (762 and 409, respectively) and the good image sensitivities ($\sim 2 \times 10^{-20}$ erg s^{-1} cm^{-2} arcsec^{-2}).

Again, a major update compared to Kakuma et al. (2021) is that we newly apply the intensity mapping technique to the CHORUS data to investigate extended Lyα emission at $z = 2.2$–3.3. In particular, we identify extended Lyα emission

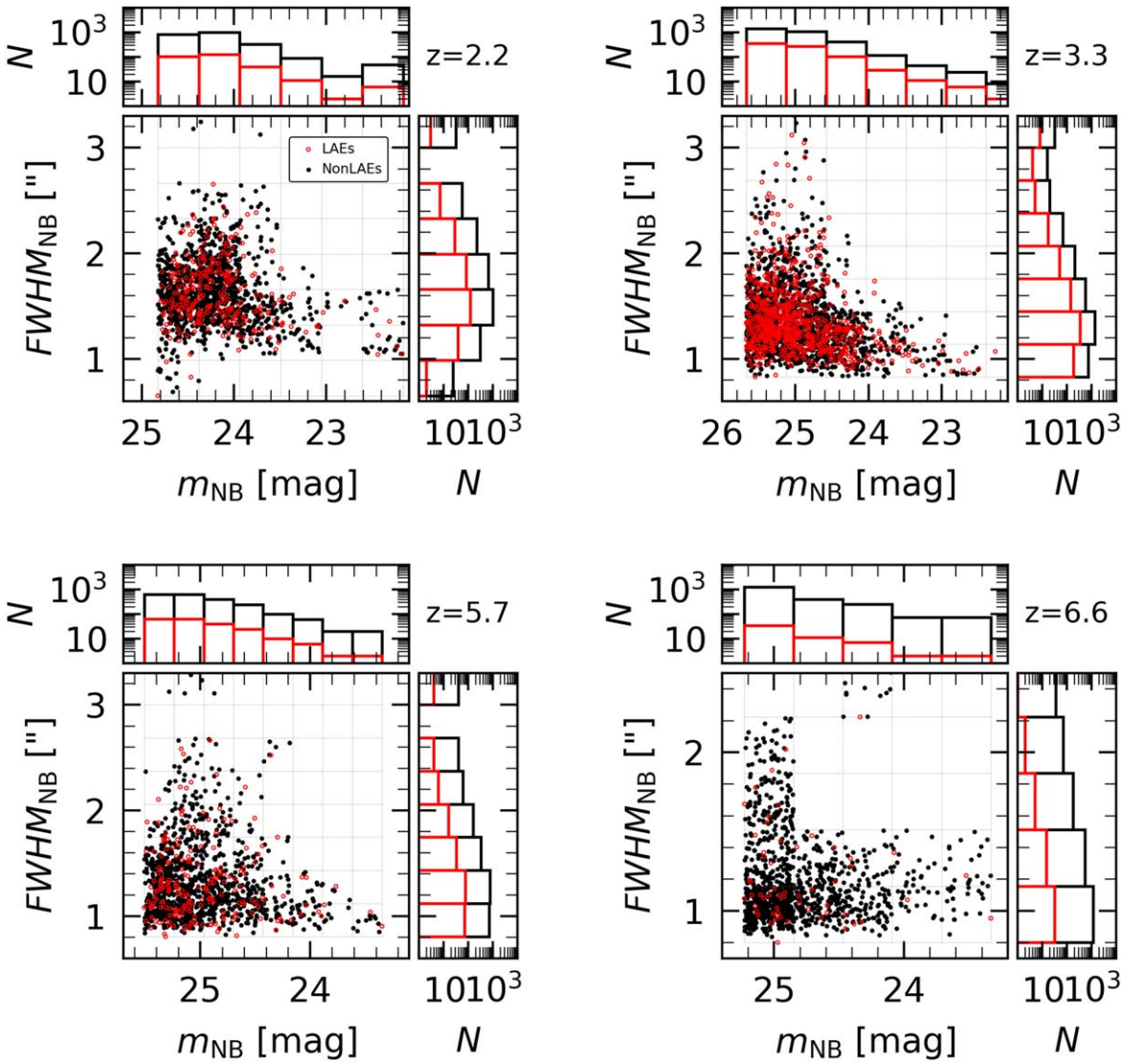

Figure 4. The $\mathrm{FWHM_{NB}}$–m_{NB} distributions of the NonLAEs defined for the *all* sample LAEs at $z = 2.2$ (top left), 3.3 (top right), 5.7 (bottom left), and 6.6 (bottom right) in the UD-COSMOS field. In each panel, the red and black circles represent the distributions of the LAEs and the corresponding NonLAEs, respectively. We also present the histograms of $\mathrm{FWHM_{NB}}$ and m_{NB} on the right and top, respectively, for the LAEs (red) and NonLAEs (black).

around the $z = 3.3$ LAEs with S/N levels comparable to or higher than those at $z = 5.7$ and 6.6. Our results at $z = 5.7$ and 6.6 are consistent with those obtained in Kakuma et al. (2021), which is as expected from similar properties of the LAEs of Kakuma et al. (2021) and our *all* sample, such as N_{LAE}, the L_{Lya} ranges, and the sky distributions (Section 2.2). In the next section, we compare our results with previous work, including Kakuma et al. (2021), in more detail.

We find that the values of $\mathrm{SB_{NB}}$ do not agree between the UD-COSMOS and UD-SXDS fields at $z = 5.7$ and 6.6. The cause of this deviation remains unclear; one possibility is that the deviation is attributed to the large variation in the IGM neutral fraction at high redshifts (e.g., Becker et al. 2015, 2018; Bosman et al. 2018; Kulkarni et al. 2019). Nonetheless, we cannot rule out that the deviation is caused by other systematics. Although we cannot find any systematics to bias our results (see the various tests in Section 2.3), we may still need to examine any other unknown systematics in an independent study.

3.3. Comparison with Previous Work

We compare our $\mathrm{SB_{Ly\alpha}}$ radial profiles with those of previous studies at $z \sim 2.2$, 3.3, 5.7, and 6.6 (Figure 9). We compile the data taken from Momose et al. (2014, 2016), Leclercq et al. (2017), Wisotzki et al. (2018), Wu et al. (2020), and Kakuma et al. (2021), which are summarized in Table 3. Because SB is affected by the cosmological dimming effect, all of the $\mathrm{SB_{Ly\alpha}}$ profiles, including ours, are scaled by $(1+z)^{-4}$ to $z = 2.2$, 3.3, 5.7, and 6.6 in each panel. We also shift the radii of the $\mathrm{SB_{Ly\alpha}}$ profiles in units of cpkc by $(1+z)$, while fixing the radii in pkpc. For our results at $z = 5.7$ and 6.6, we hereafter present $\mathrm{SB_{Ly\alpha}}$ averaged at each redshift over the UD-COSMOS and UD-SXDS fields with weights of the inverse of the $\mathrm{SB_{NB}}$ uncertainties. The uncertainties of $\mathrm{SB_{NB}}$ in the two fields are added in quadrature.

Although the $\mathrm{SB_{Ly\alpha}}$ profiles are measured under different seeing sizes, the typical image PSF FWHMs are as small as $\lesssim 1\farcs5$, corresponding to $\lesssim$40–60 ckpc at $z = 2$–7 (e.g., Momose et al. 2014; Ono et al. 2021). Since we focus on $\mathrm{SB_{Ly\alpha}}$ profiles at

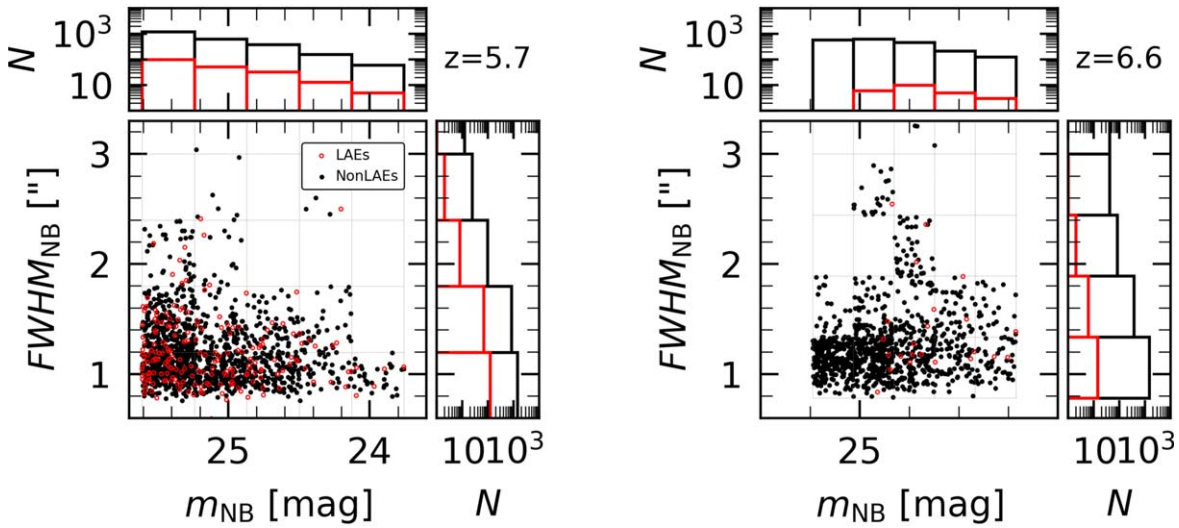

Figure 5. Same as Figure 4 but for the UD-SXDS field.

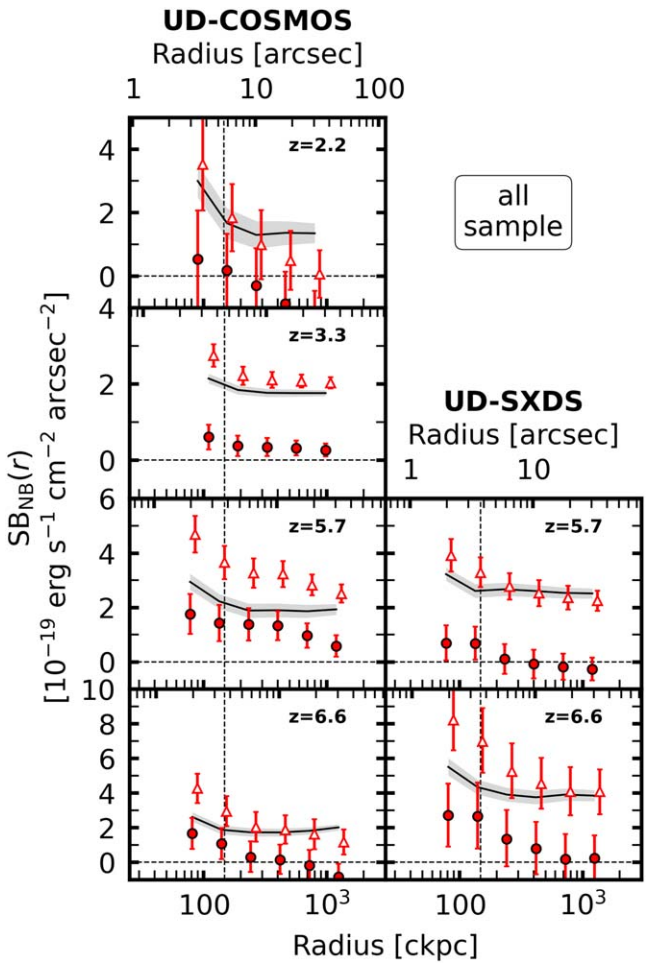

Figure 6. SB radial profiles of the *all* sample. Left: SB_{NB} in the UD-COSMOS field at $z = 2.2$, 3.3, 5.7, and 6.6, from top to bottom. The red triangles and circles show SB before and after systematics subtraction ($SB_{NB\times LAE}$ and SB_{NB}), respectively. The black solid lines represent the systematics that are estimated with the NonLAEs ($SB_{NB\times NonLAE}$). The red error bars and gray shaded area are the 1σ uncertainties estimated by the bootstrap method. The vertical black dashed line represents R_{vir} of a DMH with $M_{halo} = 10^{11}\ M_{\odot}$, while the horizontal black line represents SB = 0. The data points of $SB_{NB\times LAE}$ are slightly shifted along the horizontal axis for clarity. Right: same as the left column but in the UD-SXDS field at $z = 5.7$ and 6.6 in the top and bottom panels, respectively.

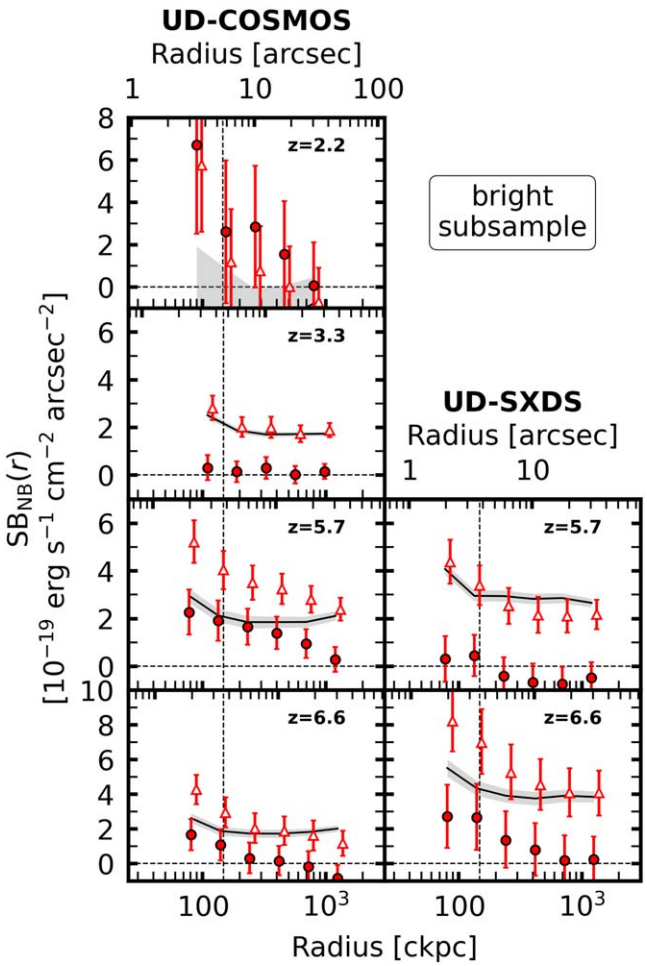

Figure 7. Same as Figure 6 but for the *bright* subsample. Note that the results at $z = 6.6$ (bottom panels) are the same as those in Figure 6, since we also treat the *all* sample also as the *bright* subsample at $z = 6.6$.

larger scales of $\gtrsim$100 ckpc, PSF differences are unlikely to affect the following discussion.

Momose et al. (2016) found that $SB_{Ly\alpha}$ profiles depend on the $L_{Ly\alpha}$ of the galaxy. To avoid this dependency, we take the data from Momose et al. (2014, 2016) and Kakuma et al. (2021)

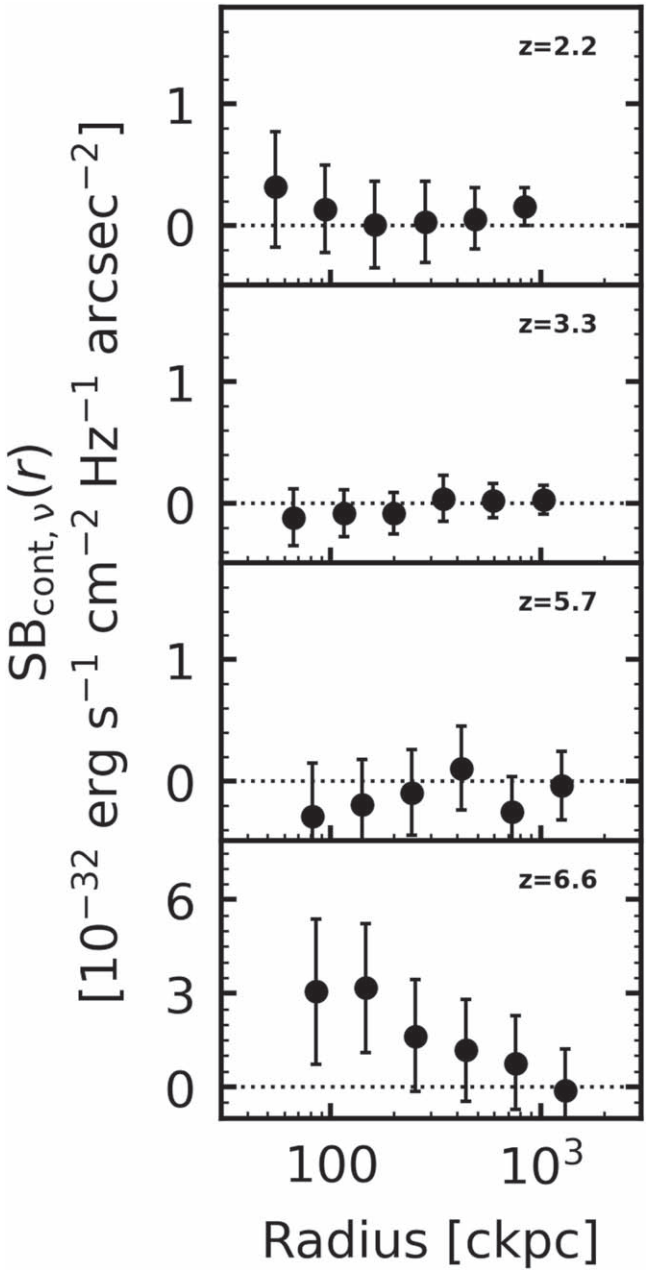

Figure 8. Radial profiles of $SB_{cont,\nu}$ of the *all* sample at $z = 2.2$, 3.3, 5.7, and 6.6 (from top to bottom). The data points should be treated as upper limits, since $SB_{cont,\nu}$ neglects signals from the PSF.

because their LAEs have $L_{Ly\alpha}$ values similar to those of our *all* samples in the same 2″ diameter aperture size. We additionally take the data from Leclercq et al. (2017), Wisotzki et al. (2018), and Wu et al. (2020), but these samples have different $L_{Ly\alpha}$ values measured in different aperture sizes. Therefore, for precise comparisons, we normalize the $SB_{Ly\alpha}$ profiles of these samples such that $SB_{Ly\alpha}$ integrated over a central 2″ diameter aperture ($=4\pi d_L^2 \int_{0''}^{1''} SB_{Ly\alpha}(r) \cdot 2\pi r dr$) becomes equal to the $L_{Ly\alpha}$ of our *all* sample at each redshift.

The top left panel in Figure 9 presents $SB_{Ly\alpha}$ radial profiles at $z = 2.2$. We compare the results of Momose et al. (2016; $L_{Ly\alpha} = 10^{42.6}$ erg s^{-1} subsample) against our *all* sample. We find that the $SB_{Ly\alpha}$ profile of Momose et al. (2016) is in good agreement with that of our *all* sample at $r \sim 100$ ckpc.

In the top right panel of Figure 9, we show the $SB_{Ly\alpha}$ profiles at $z = 3.3$. We compare the results of Momose et al. (2014; $z = 3.1$ LAEs), Leclercq et al. (2017; an individual LAE MUSE#106), Wisotzki et al. (2018; $L_{Ly\alpha} > 10^{42}$ erg s^{-1} subsample at $z = 3$–4), and our *all* sample. The $SB_{Ly\alpha}$ profiles from the literature approximately agree with that of our *all* sample even at $r \sim R_{vir}$. We additionally show the results from a subsample of Matsuda et al. (2012) with continuum magnitudes $BV \equiv (2B + V)/3$ of $26 < BV < 27$ (typical values for LAEs), where B and V are Subaru/SC B- and V-band magnitudes. The $SB_{Ly\alpha}$ profile of Matsuda et al. (2012) also agrees with that of our *all* sample around $r \sim R_{vir}$. We note that, although the results of Leclercq et al. (2017) are represented by their individual LAE MUSE#6905, their LAEs have similar $SB_{Ly\alpha}$ profiles when the amplitudes are normalized to match the $L_{Ly\alpha}$ values at $r \leqslant 1''$.

The $SB_{Ly\alpha}$ profiles at $z = 5.7$ are displayed in the bottom left panel of Figure 9. We compare the results of Momose et al. (2014; $z = 5.7$ LAEs), Leclercq et al. (2017; an individual LAE MUSE#547), Wisotzki et al. (2018; $L_{Ly\alpha} > 10^{42}$ erg s^{-1} subsample at $z = 5$–6), Wu et al. (2020; $z = 5.7$ LAEs), Kakuma et al. (2021; $z = 5.7$ LAEs), and our *all* sample. The $SB_{Ly\alpha}$ profile of our *all* sample agrees well with those of Momose et al. (2014), Leclercq et al. (2017), Wisotzki et al. (2018), and Wu et al. (2020) at $r \sim 80$–200 ckpc and that of Kakuma et al. (2021) up to $r \sim 10^3$ ckpc.

The bottom right panel of Figure 9 shows $SB_{Ly\alpha}$ profiles at $z = 6.6$ taken from Momose et al. (2014; $z = 6.6$ LAEs), Kakuma et al. (2021; $z = 6.6$ LAEs), and our *all* sample. The $SB_{Ly\alpha}$ profile of our *all* sample is consistent with those of Momose et al. (2014) and Kakuma et al. (2021) up to scales of $r \sim 100$ ckpc and 10^3 ckpc, respectively.

In summary, our $SB_{Ly\alpha}$ profiles are in good agreement with those of the previous studies at each redshift, provided that the LAEs have similar $L_{Ly\alpha}$ values at $r \leqslant 1''$. Our $SB_{Ly\alpha}$ profiles ($r \gtrsim 80$ ckpc) are smoothly connected with the inner ($r \lesssim 100$ ckpc) profiles taken from the literature at ∼100 ckpc and extend to much larger scales.

In Figure 10, we compare the $SB_{cont,\nu}$ radial profiles between Momose et al. (2014, 2016) and our *all* sample at $z = 2.2$, 3.3, and 5.7 (the data of Momose et al. 2014, 2016 are of the same LAEs as used in Figure 9). We find that the $SB_{cont,\nu}$ profiles roughly agree at $r \lesssim 400$ ckpc, although the uncertainties are large. The $SB_{cont,\nu}$ profiles are much less extended than the $SB_{Ly\alpha}$ profiles, which was also suggested by Momose et al. (2014, 2016) and Wu et al. (2020). We note that the profiles at $z = 6.6$ are not compared here because our sample is ∼0.3 dex brighter than that of Momose et al. (2014).

4. Discussion

4.1. Redshift Evolution of Extended Lyα Emission Profiles

In this section, we investigate the redshift evolution of $SB_{Ly\alpha}$ profiles of extended Lyα emission. In Figure 11, we compare the $SB_{Ly\alpha}$ profiles of our *bright* subsample at $z = 2.2$–6.6 as a function of radius in units of ckpc. We also present the results taken from Momose et al. (2014; $z = 5.7$ and 6.6 LAEs) and Wisotzki et al. (2018; $L_{Ly\alpha} > 10^{42}$ erg s^{-1} subsample at $z = 3$–4). Because our *bright* subsamples have uniform $L_{Ly\alpha}$ values ($\sim 10^{42.9}$–$10^{43.0}$ erg s^{-1}) over $z = 2.2$–6.6, the $L_{Ly\alpha}$ differences between the redshifts are unlikely to influence the following discussion.

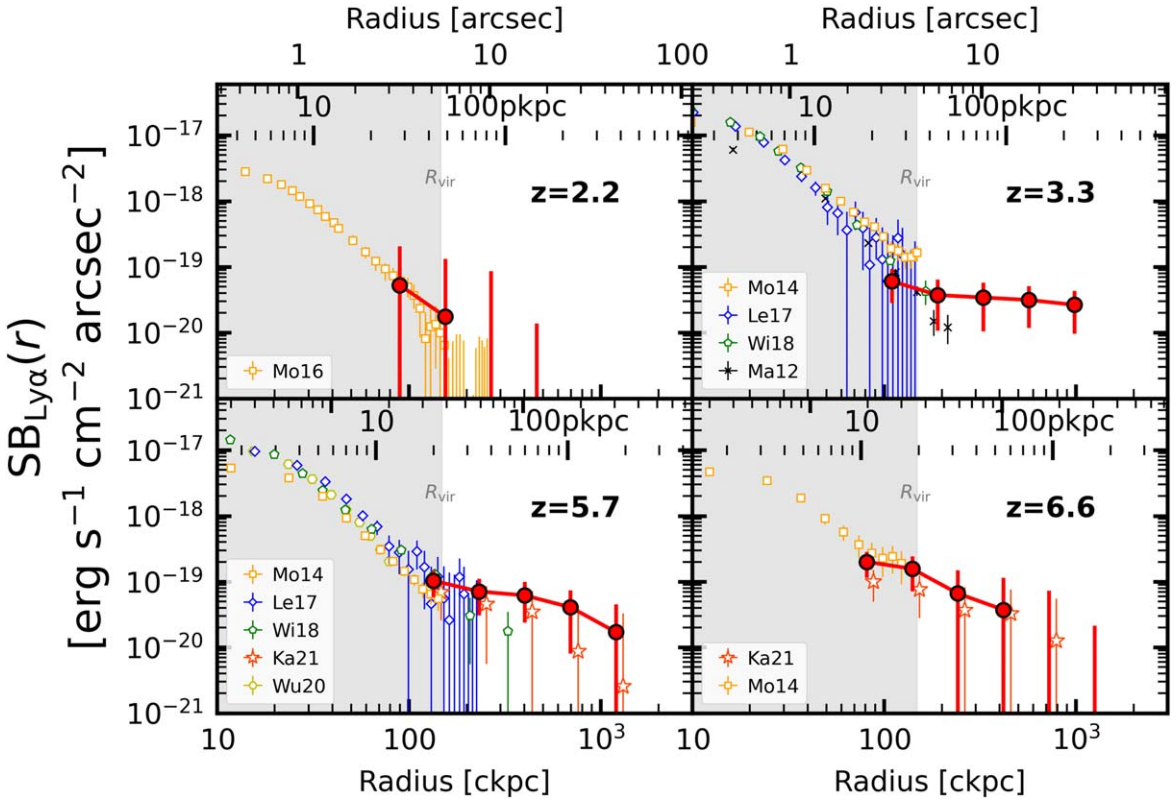

Figure 9. Comparison of the $SB_{Ly\alpha}$ radial profiles at $z = 2.2$ (top left), 3.3 (top right), 5.7 (bottom left), and 6.6 (bottom right). All of the $SB_{Ly\alpha}$ profiles are corrected by $(1+z)^{-4}$ to match each redshift. The gray shaded area illustrates the regions whose radius is smaller than the R_{vir} of a DMH with $M_{halo} = 10^{11}\,M_{\odot}$. The filled red circles show the $SB_{Ly\alpha}$ profiles of our *all* sample. The other red symbols represent the profiles taken from previous studies: Matsuda et al. (2012; Ma12, black crosses), Momose et al. (2014, 2016; Mo14, orange squares), Leclercq et al. (2017; Le17, blue diamonds), Wisotzki et al. (2018; Wi18, green pentagons), Wu et al. (2020; Wu20, yellow hexagons), and Kakuma et al. (2021; Ka21, red stars). See Table 3 for details of these samples. We omit the data points below the detection limits defined in the literature. The $SB_{Ly\alpha}$ profiles taken from Leclercq et al. (2017), Wisotzki et al. (2018), and Wu et al. (2020) are normalized such that $L_{Ly\alpha}$ values measured in a central 2″ diameter are equal to those of our *all* sample at each redshift. Some data points are slightly shifted along the horizontal axes for clarity.

The top panel of Figure 11 shows the observed $SB_{Ly\alpha}$ profiles. We identify no significant difference among the $SB_{Ly\alpha}$ profiles beyond the 1σ uncertainties at $r \sim 10^2$–10^3 ckpc over $z = 2.2$–6.6, while the uncertainties are large. This finding is consistent with that of Kakuma et al. (2021) at $z = 5.5$–6.6. There is also no significant difference in the profiles at $r < 100$ ckpc, which was also suggested by MUSE observations (Leclercq et al. 2017; see also Figure 11 of Byrohl et al. 2021) at $3 < z < 6$.

The observed $SB_{Ly\alpha}$ profiles are affected by the cosmological dimming effect. To correct this effect, we shift the observed $SB_{Ly\alpha}$ profiles vertically by $(1+z)^4/(1+3.3)^4$ and horizontally by $(1+3.3)/(1+z)$, which are hereafter termed as the intrinsic profiles (we match the profiles to $z = 3.3$ just for visibility). The intrinsic profiles are presented in the bottom panel of Figure 11. There is a tentative increasing trend in the intrinsic profiles toward $z = 6.6$, although those at $z = 2.2$ and 3.3 remain comparable due to the large uncertainties.

To quantitatively investigate the evolution, we derive the $SB_{Ly\alpha}$ intrinsic profile amplitudes at $r = 200$ ckpc ($SB_{Ly\alpha,intr}$) as a function of redshift. We fit the relation with $SB_{Ly\alpha,intr} \propto (1+z)^b$, where b is a constant, weighting by the inverse of the uncertainties of $SB_{Ly\alpha,intr}$. We find that the best-fit value is $b = 2.4 \pm 1.4$, which is consistent with the increase of the intrinsic $SB_{Ly\alpha}$ profile amplitudes toward high redshifts by $(1+z)^3$ at a given radius in units of ckpc. This trend might correspond to the increasing density of hydrogen gas toward high redshifts due to the evolution of the cosmic volume. Nevertheless, it is still difficult to draw a conclusion due to large uncertainties. We cannot rule out other possibilities, such as higher Lyα escape fractions toward high redshifts (e.g., Hayes et al. 2011; Konno et al. 2016). We also need to investigate the potential impact of the cosmic reionization on the neutral hydrogen density at $r \sim 10^2$–10^3 ckpc around LAEs. Deeper observations in the future will help to elucidate the evolution and its physical interpretation.

4.2. Physical Origins of Extended Lyα Emission

In this section, we compare the observational results obtained in Section 3 with theoretical models taken from the literature to investigate the mechanism of extended Lyα emission production. We investigate extended Lyα emission focusing on (1) where Lyα photons originate, (2) which processes produce Lyα photons, and (3) how these photons transfer in the surrounding materials.

(1) First, we distinguish Lyα emission according to where it originates from:

1. the ISM of the targeted galaxy (central galaxy),
2. the CGM surrounding the central galaxy,
3. satellite galaxies, or
4. other halos, which refer to halos distinct from that hosting the central galaxy.

Table 3
Summary of the Observational Studies Used for Comparison

Reference (1)	z (2)	$L_{\mathrm{Ly}\alpha}$ (3)	Sample (4)	Method (5)
$z\sim2.2$				
This work (*all* sample)	2.2	42.5	289 LAEs	Intensity mapping (mean)
Momose et al. (2016)	2.2	42.6	710 LAEs ($L_{\mathrm{Ly}\alpha}\geqslant10^{42.4}$ erg s^{-1})	Stacking (mean)
$z\sim3.3$				
This work (*all* sample)	3.3	42.5	762 LAEs	Intensity mapping (mean)
Momose et al. (2014)	3.1	42.7	316 LAEs	Stacking (mean)
Leclercq et al. (2017)	3.28	[42.5]	LAE MUSE#106[a]	Individual detection
Wisotzki et al. (2018)	3–4	[42.5]	18 LAEs ($L_{\mathrm{Ly}\alpha}>10^{42}$ erg s^{-1})	Stacking (median)
Matsuda et al. (2012)	3.1	⋯	894 LAEs ($26<BV<27$)[†]	Stacking (median)
$z\sim5.7$				
This work (*all* sample)	5.7	42.8	650 LAEs	Intensity mapping (mean)
Momose et al. (2014)	5.7	42.7	397 LAEs	Stacking (mean)
Leclercq et al. (2017)	5.98	[42.8]	LAE MUSE#547[a]	Individual detection
Wisotzki et al. (2018)	5–6	[42.8]	6 LAEs ($L_{\mathrm{Ly}\alpha}>10^{42}$ erg s^{-1})	Stacking (median)
Wu et al. (2020)	5.7	[42.8]	310 LAEs	Stacking (median)
Kakuma et al. (2021)	5.7	42.9	425 LAEs	Intensity mapping (mean)
$z\sim6.6$				
This work (*all* sample)	6.6	43.0	80 LAEs	Intensity mapping (mean)
Momose et al. (2014)	6.6	42.7	119 LAEs	Stacking (mean)
Kakuma et al. (2021)	6.6	42.8	396 LAEs	Intensity mapping (mean)

Notes. Columns: (1) Reference. (2) Redshift. (3) Mean or median Lyα luminosity of the sample within a 2″ diameter aperture in units of log erg s^{-1}. We normalize the $\mathrm{SB}_{\mathrm{Ly}\alpha}$ profiles of Leclercq et al. (2017), Wisotzki et al. (2018), and Wu et al. (2020) such that $\mathrm{SB}_{\mathrm{Ly}\alpha}$ integrated over a central 2″ diameter aperture becomes equal to the $L_{\mathrm{Ly}\alpha}$ of our *all* sample at each redshift, which is indicated by the brackets. (4) Sample used for comparison. The parentheses indicate specific subsamples. (5) Method for deriving the $\mathrm{SB}_{\mathrm{Ly}\alpha}$ profiles.
[a] ID of the individual LAE. See Section 3.3 for the variance among the individual LAEs.

(2) We consider that Lyα photons are produced in the processes of recombination and/or collisional excitation (cooling radiation), as stated in the Introduction.

(3) Lastly, Lyα photons subsequently transfer through surrounding hydrogen gas while being resonantly scattered, which affects the observed SB profiles. Hence, we should be conscious of whether the models take into account the scattering process or not (see Byrohl et al. 2021 for the impact of scattering on $\mathrm{SB}_{\mathrm{Ly}\alpha}$ profiles).

In Figure 12, we compare the $\mathrm{SB}_{\mathrm{Ly}\alpha}$ profiles that are observed (Section 3.2) and those predicted by theoretical work. The observational results are taken from Momose et al. (2016; $L_{\mathrm{Ly}\alpha}=10^{42.6}$ erg s^{-1} subsample at $z=2.2$), Wisotzki et al. (2018; $L_{\mathrm{Ly}\alpha}>10^{42}$ erg s^{-1} subsample at $z=3$–4), Momose et al. (2014; $z=5.7$ and 6.6 LAEs), and our *all* samples ($z=2.2$–6.6). Predicted profiles are taken from Zheng et al. (2011), Dijkstra & Kramer (2012), Lake et al. (2015), Mas-Ribas et al. (2017b), Kakiichi & Dijkstra (2018), and Byrohl et al. (2021) and are summarized in Table 4. We plot these observational and theoretical results at the nearest redshifts among $z=2.2$, 3.3, 5.7, and 6.6, except that the model of Mas-Ribas et al. (2017b) is presented at all redshifts, with the correction for the cosmological dimming effect. We normalize all of the profiles such that they match at $r=1''$ in amplitude for precise comparison under the same Lyα luminosity of the central galaxy (the models of Zheng et al. 2011, Lake et al. 2015, and Byrohl et al. 2021 are normalized in each total profile summing up different origins). We compare these observational and theoretical results in the context of the Lyα photon origins in the following subsections.

4.2.1. Central Galaxy

To discuss the contribution from the central galaxy, we compare the models of Zheng et al. (2011), Dijkstra & Kramer (2012), Lake et al. (2015), Kakiichi & Dijkstra (2018), and Byrohl et al. (2021). They applied Lyα radiative transfer modeling to hydrodynamic cosmological galaxy formation simulations at $z=5.7$, 3.1, 2–3, and 2–5, respectively, to investigate Lyα photons produced by star formation in the central galaxy and resonantly scattered into the CGM. We take the "one-halo" term model from Zheng et al. (2011), where Lyα photons are scattered not only in the CGM but also in the IGM. The model of Lake et al. (2015) takes into account the contribution from cooling radiation in addition to that from star formation. The model of Kakiichi & Dijkstra (2018) is taken in an approximated form of their Equation (28). The model of Byrohl et al. (2021) considers recombination caused by ionizing photons from star formation and UVB, as well as cooling via collisional de-excitation.

The black lines in Figure 12 represent the contribution from the central galaxy: Kakiichi & Dijkstra (2018; dotted, $z=2.2$), Byrohl et al. (2021; solid, $z=3.3$), Lake et al. (2015; dashed–dotted, $z=3.3$), Dijkstra & Kramer (2012; dotted, $z=3.3$), and Zheng et al. (2011; solid, $z=5.7$). These models successfully reproduce the observed $\mathrm{SB}_{\mathrm{Ly}\alpha}$ profiles inside the CGM ($r<R_{\mathrm{vir}}$) at $z=3.3$ and 5.7, implying resonant scattering as a major source powering Lyα emission. This finding is also supported by previous studies in other aspects, such as halo properties (e.g., a halo luminosity–mass relation; Kusakabe et al. 2019) and kinematics (e.g., a correlation between the peak

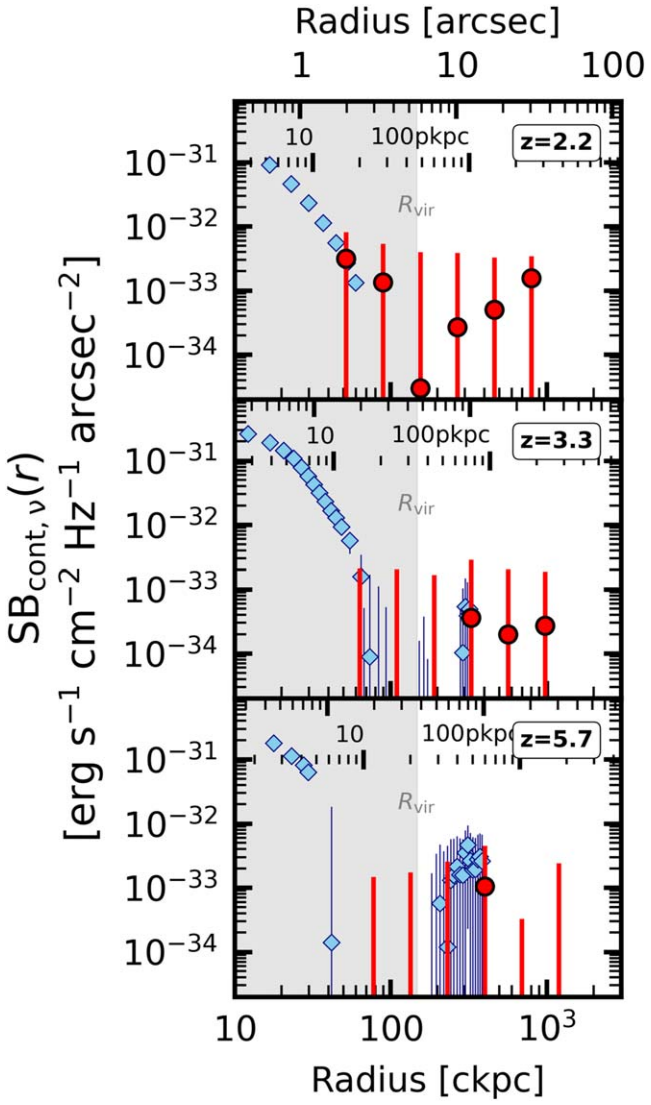

Figure 10. Comparison of the $\mathrm{SB_{cont,\nu}}$ radial profiles at $z = 2.2$ (top), 3.3 (middle), and 5.7 (bottom). The red circles and cyan diamonds show the $\mathrm{SB_{cont,\nu}}$ profiles of our *all* sample and Momose et al. (2014, 2016), respectively (we use the data of Momose et al. (2014, 2016) at $z = 3.3$ and 5.7, respectively). The data of Momose et al. (2014) at $z = 3.1$ are plotted at $z = 3.3$ with the correction of $(1 + z)^{-4}$. The gray shaded area illustrates the regions inside the $R_{\rm vir}$ of a DMH with $M_{\rm halo} = 10^{11}\ M_\odot$.

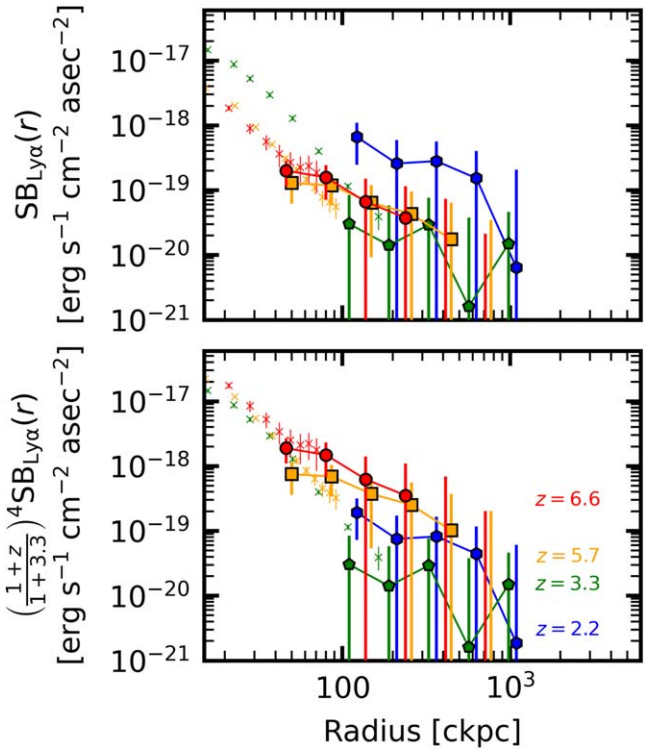

Figure 11. Comparison between $\mathrm{SB_{Ly\alpha}}$ radial profiles at $z = 2.2$–6.6. Top: observed $\mathrm{SB_{Ly\alpha}}$ profiles. The blue hexagons, green pentagons, orange squares, and red circles represent the profiles of our *bright* subsamples at $z = 2.2$, 3.3, 5.7, and 6.6, respectively. The green, orange, and red crosses denote profiles taken from Wisotzki et al. (2018), Momose et al. (2014), and Momose et al. (2014), which are normalized to $z = 3.3$, 5.7, and 6.6, respectively. The $\mathrm{SB_{Ly\alpha}}$ profile of Wisotzki et al. (2018) is normalized such that $L_{\rm Lya}$ in $r \leqslant 1''$ matches that of our *all* sample (see Section 3.3). We again note that our profiles here are based on *bright* subsamples and thus differ from those shown in Figure 9. Bottom: same as the top panel but showing the profiles corrected for the cosmological dimming effect, i.e., the intrinsic $\mathrm{SB_{Ly\alpha}}$ profiles.

velocity shift and the width of a Lyα line, Leclercq et al. 2020; and red peak-dominated Lyα spectra, Chen et al. 2021).

The one-halo term of Zheng et al. (2011) also reproduces the observed $\mathrm{SB_{Ly\alpha}}$ profile from $r \sim R_{\rm vir}$ to $\sim 10^3$ ckpc at $z = 5.7$. Their model takes into account resonant scattering in the IGM in addition to that in the CGM. This effect leads to a plateau-like feature in an $\mathrm{SB_{Ly\alpha}}$ profile at $r \sim 300$–10^3 ckpc (see also Jeeson-Daniel et al. 2012), which is indeed observed at $z = 3.3$ and 5.7. Therefore, we may interpret that the observed extended Lyα emission outside the CGM is produced by resonant scattering in the IGM, although the uncertainties are large. At $z = 3.3$, however, the models adopted here (Dijkstra & Kramer 2012; Lake et al. 2015; Byrohl et al. 2021) produce values lying far below the observed $\mathrm{SB_{Ly\alpha}}$ profile beyond 300 ckpc and do not reproduce a plateau-like shape, unlike the one-halo term of Zheng et al. (2011). This may indicate less neutral gas in the IGM at $z = 3.3$ compared to $z = 5.7$, which causes less frequent scattering. We cannot deny the possibility that the discrepancies are attributed to the different assumptions and incorporated physics in the models, such as treatment of stellar radiation, dust, and scattering, especially beyond $R_{\rm vir}$. Nevertheless, since the one-halo term of Zheng et al. (2011) is consistent with the observed $\mathrm{SB_{Ly\alpha}}$ profile at $z = 5.7$, we cannot rule out the possibility that scattered Lyα photons originating from the central galaxy contribute to extended Lyα emission beyond $R_{\rm vir}$. We need additional inputs on the neutral hydrogen gas distribution outside $R_{\rm vir}$ to further determine the contribution of resonant scattering.

The assumptions on the $M_{\rm halo}$ values are unlikely to affect our discussion here because the models above use roughly similar $M_{\rm halo}$ values: $10^{11.2}$ and $10^{11.5}\ M_\odot$ for Zheng et al. (2011) and Lake et al. (2015), respectively. Byrohl et al. (2021) assumed a stellar mass $M_\star$ range of $10^{8.5}$–$10^{9.5}\ M_\odot$ at $z = 3$, which corresponds to $M_{\rm halo} \sim 10^{11}\ M_\odot$ given the $M_\star/M_{\rm halo}$ ratio obtained in Behroozi et al. (2019; see also Kusakabe et al. 2018). These values are similar to those obtained in the previous observations (e.g., Ouchi et al. 2010; Kusakabe et al. 2018).

4.2.2. CGM

We next use the model from Mas-Ribas et al. (2017b) to investigate the Lyα emission produced in the CGM. They constructed an analytical model of fluorescent emission in the CGM caused by ionizing radiation from star formation in the

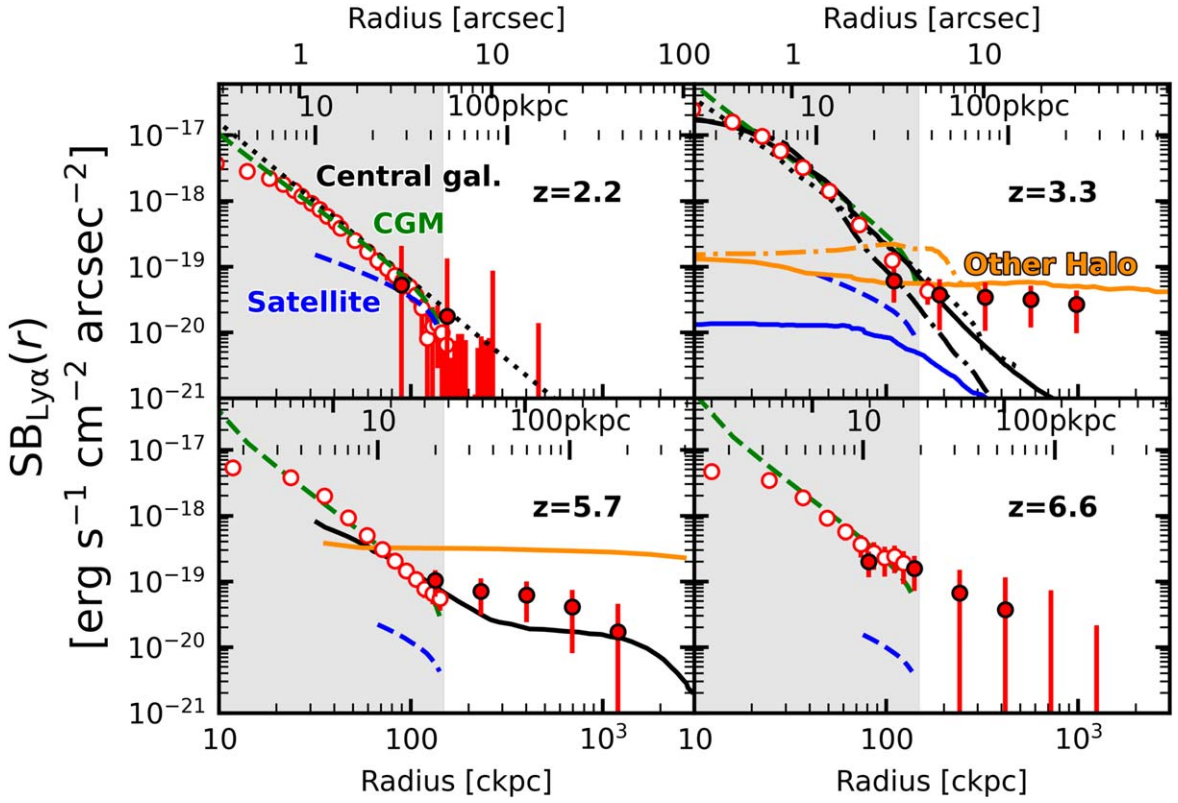

Figure 12. Comparison of the $SB_{Ly\alpha}$ radial profiles between the observational and theoretical studies at $z = 2.2$ (top left), 3.3 (top right), 5.7 (bottom left), and 6.6 (bottom right). The filled red circles depict the observational results taken from our *all* sample ($z = 2.2$–6.6), while the open red circles show the results from previous observational work (Momose et al. 2016 at $z = 2.2$, Wisotzki et al. 2018 at $z = 3.3$, and Momose et al. 2014 at $z = 5.7$ and 6.6). The $SB_{Ly\alpha}$ amplitude of Wisotzki et al. (2018) is normalized such that L_{Lya} in $r \leqslant 1''$ matches that of our *all* sample (see Section 3.3). We represent the theoretical work with the lines, whose colors indicate the origins of the Lyα emission: the central galaxy (black), CGM (green), satellite galaxies (blue), and other halos (orange). The models are taken from Mas-Ribas et al. (2017b; green and blue dashed lines at $z = 2.2$, 3.3, 5.7, and 6.6), Kakiichi & Dijkstra (2018; black dotted line at $z = 2.2$), Byrohl et al. (2021; black, blue, and orange solid lines at $z = 3.3$), Lake et al. (2015; black and orange dashed–dotted lines at $z = 3.3$), Dijkstra & Kramer (2012; black dotted line at $z = 3.3$), and Zheng et al. (2011; black and orange solid lines at $z = 5.7$). See Table 4 for details of these models. We normalize the $SB_{Ly\alpha}$ profiles from the model predictions such that the central galaxy ($r \leqslant 1''$) has a $L_{Ly\alpha}$ value similar to that observed at each redshift. The gray shaded area illustrates the regions inside the R_{vir} of a DMH with $M_{halo} = 10^{11}\ M_\odot$.

central galaxy at $z = 5.7$ and 6.6 (we also apply this model to $z = 3.3$ and 2.2; see also Mas-Ribas & Dijkstra 2016). The model of Mas-Ribas et al. (2017b) includes three free parameters: (1) CGM structure, (2) star formation rate (SFR), and (3) radius R_{max}. First, we adopt the simplified clumpy outflow model of Steidel et al. (2010) as the CGM structure (the choice here has only a small impact on the $SB_{Ly\alpha}$ profiles; see Figure 2 of Mas-Ribas & Dijkstra 2016). Second, while SFR determines the amplitude of $SB_{Ly\alpha}$, we match the amplitudes to those observed. The normalized amplitudes correspond to SFR $\sim 10\ M_\odot\ yr^{-1}$, which is close to the observed values (e.g., Ouchi et al. 2010; Nakajima et al. 2012; Kusakabe et al. 2018, 2019) and the values adopted in Mas-Ribas et al. (2017b). Third, $SB_{Ly\alpha}(b)$ is derived as the integration of Lyα emissivity at radius r over $b \leqslant r \leqslant R_{max}$, where b denotes the impact parameter (see Equations (4) and (2) of Mas-Ribas & Dijkstra 2016 and Mas-Ribas et al. 2017b, respectively). Here R_{max} represents the extent to which Lyα emission contributes to $SB_{Ly\alpha}$. We assume that R_{max} is equivalent to R_{vir} for a DMH of $M_{halo} = 10^{11}\ M_\odot$. Their model ignores the effect of resonant scattering.

The green dashed lines in Figure 12 represent the model of Mas-Ribas et al. (2017b). The $SB_{Ly\alpha}$ profiles predicted by their model are in good agreement with those observed inside R_{vir} at all redshifts. However, because the $SB_{Ly\alpha}$ profiles sharply drop at $r = R_{max}$ according to this model, the emission originating from the CGM cannot contribute to extended emission beyond R_{vir}. Mas-Ribas & Dijkstra (2016) and Mas-Ribas et al. (2017b) arbitrarily adopted much larger R_{max} values (>100 ckpc) to reproduce the profiles obtained in Momose et al. (2014), but such large R_{max} values correspond to $M_{halo} > 10^{12}\ M_\odot$, which is much larger than those observed (e.g., Ouchi et al. 2010; Kusakabe et al. 2018). If R_{max} is larger than R_{vir}, materials should exist outside the CGM ($\gtrsim$three times larger scales than R_{vir}) and produce fluorescent emission contributing to extended Lyα emission. In either case, the observed $SB_{Ly\alpha}$ profiles beyond 300 cpkc at $z = 3.3$ cannot be reproduced, even with larger values of R_{max}.

Overall, fluorescence in the CGM can power Lyα emission inside R_{vir} according to the model of Mas-Ribas et al. (2017b), while it plays only a marginal role beyond R_{vir}. This behavior was also suggested by MUSE UDF data (Gallego et al. 2018; Bacon et al. 2021). We note that the model of Mas-Ribas et al. (2017b) ignores the scattering effect, which leads to a sharp drop of $SB_{Ly\alpha}$ at $r = R_{max}$. Hence, it is necessary to incorporate resonant scattering to extend Lyα emission when we rely on the CGM fluorescence scenario.

The contribution from cooling radiation in the CGM remains unclear. Byrohl et al. (2021) argued that cooling radiation dominates ~30% of the total Lyα emission at $r \gtrsim 80$ ckpc. On

Table 4
Summary of the Theoretical Studies Used for Comparison

Reference (1)	$z_{\rm model}$ (2)	$z_{\rm plot}$ (3)	Origin (4)	Process (5)	Scattering (6)	$M_{\rm halo}$ ($M_\odot$) (7)
Mas-Ribas et al. (2017b)	5.7, 6.6	2.2, 3.3, 5.7, 6.6	CGM/sat.	Rec.	n	10^{11}[a]
Kakiichi & Dijkstra (2018)	2–3	2.2	Cen.	Rec.	y	$\sim10^{12}$
Byrohl et al. (2021)	2–5	3.3	Cen./sat./other	Rec./cool.	y	$\sim10^{11}$[b]
Dijkstra & Kramer (2012)	$\sim$2.65	3.3	Cen.	Rec.	y	...
Lake et al. (2015)	3.1	3.3	Cen./other	Rec./cool.	y	$10^{11.5}$
Zheng et al. (2011)	5.7	5.7	Cen./other	Rec.	y	$10^{11.2}$

Notes. Columns: (1) Reference. (2) Redshift assumed in the model. (3) Redshift where we plot the model in Figure 12. (4) Origins of Lyα photons (where Lyα photons are produced): the central galaxy (cen.), CGM, satellite galaxies (sat.), and other halos (other). (5) Physical processes of Lyα emission production (how Lyα emission is produced): recombination (rec.) and cooling radiation (cool.). (6) Whether or not the model takes into account Lyα radiative transfer (i.e., resonant scattering). (7) Assumed halo mass in units of $M_\odot$.
[a] We fix $M_{\rm halo}$ to 10^{11} $M_\odot$, while $M_{\rm halo}$ is a free parameter in the model.
[b] This value was converted from the assumed stellar mass $M_\star$ of $10^{8.5}$–$10^{9.5}$ $M_\odot$ with the $M_\star/M_{\rm halo}$ ratio obtained in Behroozi et al. (2019).

the other hand, Rosdahl & Blaizot (2012) found that Lyα emission from cooling radiation is centrally ($r<40$ ckpc) concentrated for a DMH with $M_{\rm halo}=10^{11}$ $M_\odot$. We need additional models at larger scales to further discuss whether cooling radiation contributes to extended Lyα emission or not.

4.2.3. Satellite Galaxies

We adopt another model from Mas-Ribas et al. (2017b) that predicts the contribution from star formation in satellite galaxies (see also Mas-Ribas et al. 2017a). There are three free parameters in their model: (1) a clustering description, (2) a Lyα escape fraction ($f_{\rm Lya}^{\rm esc}$), and (3) $R_{\rm max}$. First, we assume that clustering follows a power-law two-point cross-correlation function $\xi(r)$ of $\xi(r)=(r/r_0)^{-\alpha}$ with scale length $r_0=400$ ckpc and index $\alpha=1.8$ (e.g., Ouchi et al. 2010; Harikane et al. 2016; Bielby et al. 2017). Second, we fix $f_{\rm Lya}^{\rm esc}$ to 0.4 (Steidel et al. 2010), while $\mathrm{SB_{Ly\alpha}}$ linearly depends on $f_{\rm Lya}^{\rm esc}$. Third, satellite galaxies are assumed to exist from $r=10$ pkpc to $R_{\rm max}$, which we assume to be equal to $R_{\rm vir}$ in the same way as for the fluorescence model (Section 4.2.2). We additionally take the "outer halo" model from Byrohl et al. (2021).

The blue dashed and solid lines represent the models of Mas-Ribas et al. (2017b) and Byrohl et al. (2021), respectively. We find that the contributions from satellite galaxies are negligible compared to the other contributions, except at $r\sim100$ ckpc at $z=2.2$. While we choose a power-law correlation function to describe the clustering, other choices, such as the Navarro–Frenk–White profile (Navarro et al. 1997), reduce the $\mathrm{SB_{Ly\alpha}}$ values at $r>40$ ckpc (see the left panel of Figure 2 of Mas-Ribas et al. 2017a). When a power-law correlation function is assumed, larger r_0 values increase the overall profiles. However, unrealistically large values of r_0 and $R_{\rm max}$ are necessary to reproduce extended Lyα emission beyond $R_{\rm vir}$ with satellite galaxies alone. Additionally, the model overpredicts the observed $\mathrm{SB_{cont,\nu}}$ values when the model is tuned to reproduce the observed $\mathrm{SB_{Ly\alpha}}$ profiles (Mas-Ribas et al. 2017a).

For these reasons, we conclude that satellite galaxies are unlikely to contribute to extended Lyα emission beyond $R_{\rm vir}$. This conclusion is supported by the fact that emission is more extended in Lyα than in UV continuum (Section 3.2; see also Momose et al. 2014, 2016; Wu et al. 2020) because the $\mathrm{SB_{cont,\nu}}$ profiles should be extended similarly as the $\mathrm{SB_{Ly\alpha}}$ profiles if satellite galaxies contribute to $\mathrm{SB_{Ly\alpha}}$.

4.2.4. Other Halos

Lastly, we compare the models for other halos taken from Zheng et al. (2011), Lake et al. (2015), and Byrohl et al. (2021). From Lake et al. (2015), we specifically adopt the model in which Lyα emission originates from "knots," the regions with high Lyα emissivity around the central galaxy. The "two-halo" term model is taken from Zheng et al. (2011).

We show these models with the orange lines in Figure 12: Byrohl et al. (2021; solid, $z=3.3$), Lake et al. (2015; dashed–dotted, $z=3.3$), and Zheng et al. (2011; solid, $z=5.7$). At $z=3.3$, the contribution from other halos predicted by Byrohl et al. (2021) agrees with the observed $\mathrm{SB_{Ly\alpha}}$ profiles within the 1σ uncertainties. Although the knots model of Lake et al. (2015) is limited to $r\lesssim300$ cpkc, it roughly reproduces the observed profiles at $r\sim$(200–300) ckpc. On the other hand, the two-halo term of Zheng et al. (2011) at $z=5.7$ significantly overestimates the $\mathrm{SB_{Ly\alpha}}$ values beyond 100 ckpc. The amplitudes of the models of Zheng et al. (2011) and Byrohl et al. (2021) differ by $\sim$1 dex, similar to what we find in Section 4.2.1.

Kakuma et al. (2021) argued that the difference is because they masked out bright objects. However, this interpretation is not necessarily appropriate, since the profile of Byrohl et al. (2021) has an amplitude similar to (or rather slightly higher than) profiles observed at $z=3.3$. The two-halo term of Zheng et al. (2011) also overpredicts the $\mathrm{SB_{Ly\alpha}}$ values of Momose et al. (2014). Nevertheless, we cannot rule out the possibility that other halos contribute to extended Lyα emission beyond $R_{\rm vir}$, since the model of Byrohl et al. (2021) agrees with the observed $\mathrm{SB_{Ly\alpha}}$ profiles. This suggestion is consistent with Bacon et al. (2021), who identified very extended (>300 arcsec^2 or $>2\times10^4$ pkpc^2) Lyα emission at $z\sim3$ using MUSE data; they found that 70% of the total Lyα luminosity originates from filamentary structures beyond the CGM. They argued that the extended Lyα emission can be reproduced by a population of extremely faint ($<10^{40}$ erg s^{-1}) galaxies under certain conditions, which correspond to other halos in our definition.

4.2.5. Overall Interpretation

In summary, $\mathrm{SB_{Ly\alpha}}$ profiles inside the CGM ($<R_{\rm vir}$) are possibly explained by scattered Lyα emission originating from the central galaxy and/or fluorescent emission in the CGM. Meanwhile, extended Lyα emission beyond $R_{\rm vir}$ is possibly

powered by resonant scattering at large scales and/or contributed from other halos. Fluorescence in the CGM and satellite galaxies are not sufficient to reproduce the observed $SB_{Ly\alpha}$ profiles beyond R_{vir}.

We note that the processes and origins of Lyα emission may differ among LAEs. They may also vary according to the radius and redshift even when we focus on averaged profiles around different LAEs. However, our systematic investigation of extended Lyα emission at $z \sim 2-7$ is advantageous for a comprehensive understanding of the processes and origins of extended Lyα emission. More simulations focusing on large scales will help to further distinguish the processes and origins.

5. Summary

In this paper, we investigate very extended Lyα emission around LAEs at $z = 2.2$–6.6 by applying the intensity mapping technique to the Subaru/HSC-SSP and CHORUS data. We calculate cross-correlation functions between 1540 LAEs at $z = 2.2$, 3.3, 5.7, and 6.6 with Lyα emission traced by the NB387, NB527, NB816, and NB921 images. A total of ∼1–2 billion pixels are used to derive the correlation function at each redshift. The HSC deep ($m_{NB,5\sigma} \sim 26$ mag) and wide (∼4 deg^2 over the UD-COSMOS and UD-SXDS fields) images enable us to detect very diffuse Lyα emission. Our major findings are summarized as follows.

1. Subtracting the systematics, such as the sky background and PSF, with foreground objects (NonLAEs), we identify Lyα emission of $\sim 10^{-20}$–10^{-19} erg s^{-1} cm^{-2} arcsec^{-2} with S/N = 3.2 around the $z = 3.3$ LAEs. The Lyα emission extends beyond the radial scale of the R_{vir} of a DMH with 10^{11} $M_\odot$ (∼100 ckpc) and up to $\sim 10^3$ ckpc. We also detect Lyα emission beyond R_{vir} with S/N = 3.7 at $z = 5.7$ and tentatively with S/N = 2.0 at $z = 6.6$. The signal at $z = 2.2$ is very tentative even when we exclude faint LAEs.
2. We confirm that the $SB_{Ly\alpha}$ radial profiles around our LAEs agree well with those obtained in the previous studies when the LAEs have similar Lyα luminosity values.
3. We compare the observed $SB_{Ly\alpha}$ profiles across $z = 2.2$–6.6, finding no significant difference among the redshifts beyond the uncertainties. Meanwhile, there is a potential increasing trend toward high redshifts in the intrinsic $SB_{Ly\alpha}$ profiles, which are corrected for the cosmological dimming effect. The increasing trend might be explained by the increasing density of the neutral hydrogen gas due to the evolution of the cosmic volume.
4. We compare the $SB_{Ly\alpha}$ profiles obtained from the observational and theoretical studies. We find that the observed $SB_{Ly\alpha}$ profiles inside the CGM can be reproduced by the models in which Lyα photons originating from the central galaxy subsequently transfer into the CGM via resonant scattering or Lyα emission is produced in the CGM via fluorescence due to ionizing photons. Extended Lyα emission beyond R_{vir} may be reproduced by resonant scattering at large scales and/or emission originating from clustered halos around the targeted galaxy. The CGM and satellite galaxies are unlikely to contribute to extended Lyα emission beyond R_{vir}.

This work, in conjunction with the previous observational studies, might suggest that very extended diffuse Lyα emission beyond R_{vir} ubiquitously exists around LAEs at $z \sim 2-7$, not only around massive galaxies. Deeper images obtained by larger-area surveys in the future should enable further investigation of very extended Lyα emission at more diffuse levels. Applying the intensity mapping technique to the emission of multiple lines, such as Hα and [O iii], will help to further distinguish the physical processes and origins of extended Lyα emission because they trace different components (see Figures 6 and 12 of Mas-Ribas et al. 2017a and Fujimoto et al. 2019). These emission lines will be observed with next-generation facilities, such as the James Webb Space Telescope, the Nancy Grace Roman Space Telescope, and the Spectro-Photometer for the History of the Universe, Epoch of Reionization and Ices Explorer.

We thank the anonymous referee for carefully reading the manuscript and providing us with plenty of insightful comments. We are grateful to Chris Byrohl for his helpful comments and discussions, especially on simulations and physical interpretations.

The HSC collaboration includes the astronomical communities of Japan and Taiwan, and Princeton University. The HSC instrumentation and software were developed by the National Astronomical Observatory of Japan (NAOJ), the Kavli Institute for the Physics and Mathematics of the Universe (Kavli IPMU), the University of Tokyo, the High Energy Accelerator Research Organization (KEK), the Academia Sinica Institute for Astronomy and Astrophysics in Taiwan (ASIAA), and Princeton University. Funding was contributed by the FIRST program from the Japanese Cabinet Office, the Ministry of Education, Culture, Sports, Science and Technology (MEXT), the Japan Society for the Promotion of Science (JSPS), Japan Science and Technology Agency (JST), the Toray Science Foundation, NAOJ, Kavli IPMU, KEK, ASIAA, and Princeton University.

This paper makes use of software developed for Vera C. Rubin Observatory. We thank the Rubin Observatory for making their code available as free software at http://pipelines.lsst.io/.

This paper is based on data collected at the Subaru Telescope and retrieved from the HSC data archive system, which is operated by the Subaru Telescope and Astronomy Data Center (ADC) at NAOJ. Data analysis was in part carried out with the cooperation of the Center for Computational Astrophysics (CfCA), National Astronomical Observatory of Japan. The Subaru Telescope is honored and grateful for the opportunity of observing the Universe from Maunakea, which has cultural, historical, and natural significance in Hawaii.

The Pan-STARRS1 Surveys (PS1) and the PS1 public science archive have been made possible through contributions by the Institute for Astronomy, the University of Hawaii, the Pan-STARRS Project Office, the Max Planck Society and its participating institutes, the Max Planck Institute for Astronomy, Heidelberg, and the Max Planck Institute for Extraterrestrial Physics, Garching, The Johns Hopkins University, Durham University, the University of Edinburgh, the Queens University Belfast, the Harvard-Smithsonian Center for Astrophysics, the Las Cumbres Observatory Global Telescope Network Incorporated, the National Central University of Taiwan, the Space Telescope Science Institute, the National Aeronautics and Space Administration under grant No. NNX08AR22G issued through the Planetary Science Division of the NASA Science Mission Directorate, the National

Science Foundation grant No. AST-1238877, the University of Maryland, Eotvos Lorand University (ELTE), the Los Alamos National Laboratory, and the Gordon and Betty Moore Foundation.

The NB387, NB527, and NB921 filters were supported by KAKENHI (23244022, 24244018, and 23244025, respectively) Grant-in-Aid for Scientific Research (A) through the JSPS. The NB816 filter was supported by Ehime University.

This work is supported by JSPS KAKENHI Grant Numbers 17H01114, 19J01222, 20H00180, 20J11993, 21H04467, 21H04490, and 21K13953. This work is supported by the joint research program of the Institute for Cosmic Ray Research (ICRR), the University of Tokyo.

ORCID iDs

Shotaro Kikuchihara https://orcid.org/0000-0003-2449-6314
Yuichi Harikane https://orcid.org/0000-0002-6047-430X
Masami Ouchi https://orcid.org/0000-0002-1049-6658
Yoshiaki Ono https://orcid.org/0000-0001-9011-7605
Akio K. Inoue https://orcid.org/0000-0002-7779-8677
Haruka Kusakabe https://orcid.org/0000-0002-3801-434X
Kazuhiro Shimasaku https://orcid.org/0000-0002-2597-2231
Rieko Momose https://orcid.org/0000-0002-8857-2905
Yuma Sugahara https://orcid.org/0000-0001-6958-7856
Satoshi Kikuta https://orcid.org/0000-0003-3214-9128
Shun Saito https://orcid.org/0000-0002-6186-5476
Nobunari Kashikawa https://orcid.org/0000-0003-3954-4219
Haibin Zhang https://orcid.org/0000-0003-2273-9415
Chien-Hsiu Lee https://orcid.org/0000-0003-1700-5740

References

Aihara, H., AlSayyad, Y., Ando, M., et al. 2019, PASJ, 71, 114
Arrigoni Battaia, F., Hennawi, J. F., Prochaska, J. X., et al. 2019, MNRAS, 482, 3162
Bacon, R., Mary, D., Garel, T., et al. 2021, A&A, 647, A107
Becker, G. D., Bolton, J. S., Madau, P., et al. 2015, MNRAS, 447, 3402
Becker, G. D., Davies, F. B., Furlanetto, S. R., et al. 2018, ApJ, 863, 92
Behroozi, P., Wechsler, R. H., Hearin, A. P., & Conroy, C. 2019, MNRAS, 488, 3143
Bertin, E., & Arnouts, S. 1996, A&AS, 117, 393
Bielby, R. M., Shanks, T., Crighton, N. H. M., et al. 2017, MNRAS, 471, 2174
Blanton, M. R., Bershady, M. A., Abolfathi, B., et al. 2017, AJ, 154, 28
Bond, N. A., Feldmeier, J. J., Matković, A., et al. 2010, ApJL, 716, L200
Borisova, E., Cantalupo, S., Lilly, S. J., et al. 2016, ApJ, 831, 39
Bosch, J., Armstrong, R., Bickerton, S., et al. 2018, PASJ, 70, S5
Bosman, S. E. I., Fan, X., Jiang, L., et al. 2018, MNRAS, 479, 1055
Byrohl, C., Nelson, D., Behrens, C., et al. 2021, MNRAS, 506, 5129
Cantalupo, S., Arrigoni-Battaia, F., Prochaska, J. X., Hennawi, J. F., & Madau, P. 2014, Natur, 506, 63
Cantalupo, S., Porciani, C., Lilly, S. J., & Miniati, F. 2005, ApJ, 628, 61
Carilli, C. L. 2011, ApJL, 730, L30
Chen, Y., Steidel, C. C., Erb, D. K., et al. 2021, MNRAS, 508, 19
Comaschi, P., & Ferrara, A. 2016a, MNRAS, 463, 3078
Comaschi, P., & Ferrara, A. 2016b, MNRAS, 455, 725
Croft, R. A. C., Miralda-Escudé, J., Zheng, Z., et al. 2016, MNRAS, 457, 3541
Croft, R. A. C., Miralda-Escudé, J., Zheng, Z., Blomqvist, M., & Pieri, M. 2018, MNRAS, 481, 1320
Dawson, K. S., Schlegel, D. J., Ahn, C. P., et al. 2013, AJ, 145, 10
Dijkstra, M., & Kramer, R. 2012, MNRAS, 424, 1672
Eisenstein, D. J., Weinberg, D. H., Agol, E., et al. 2011, AJ, 142, 72
Fardal, M. A., Katz, N., Gardner, J. P., et al. 2001, ApJ, 562, 605
Faucher-Giguère, C.-A., Kereš, D., Dijkstra, M., Hernquist, L., & Zaldarriaga, M. 2010, ApJ, 725, 633
Feldmeier, J. J., Hagen, A., Ciardullo, R., et al. 2013, ApJ, 776, 75
Fisher, R., & Aylmer, S. 1970, Statistical Methods for Research Workers (14th ed.; Edinburgh: Oliver and Boyd)
Fonseca, J., Silva, M. B., Santos, M. G., & Cooray, A. 2017, MNRAS, 464, 1948
Fujimoto, S., Ouchi, M., Ferrara, A., et al. 2019, ApJ, 887, 107
Furlanetto, S. R., Schaye, J., Springel, V., & Hernquist, L. 2005, ApJ, 622, 7
Gaia Collaboration, Brown, A. G. A., Vallenari, A., et al. 2018, A&A, 616, A1
Gallego, S. G., Cantalupo, S., Lilly, S., et al. 2018, MNRAS, 475, 3854
Garel, T., Blaizot, J., Rosdahl, J., et al. 2021, MNRAS, 504, 1902
Goerdt, T., Dekel, A., Sternberg, A., et al. 2010, MNRAS, 407, 613
Gong, Y., Cooray, A., Silva, M. B., Santos, M. G., & Lubin, P. 2011, ApJL, 728, L46
Goto, T., Utsumi, Y., Furusawa, H., Miyazaki, S., & Komiyama, Y. 2009, MNRAS, 400, 843
Haiman, Z., Spaans, M., & Quataert, E. 2000, ApJL, 537, L5
Harikane, Y., Ouchi, M., Ono, Y., et al. 2016, ApJ, 821, 123
Hayashi, M., Shimakawa, R., Tanaka, M., et al. 2020, PASJ, 72, 86
Hayashino, T., Matsuda, Y., Tamura, H., et al. 2004, AJ, 128, 2073
Hayes, M., Östlin, G., Duval, F., et al. 2014, ApJ, 782, 6
Hayes, M., Östlin, G., Schaerer, D., et al. 2013, ApJL, 765, L27
Hayes, M., Schaerer, D., Östlin, G., et al. 2011, ApJ, 730, 8
Inoue, A. K., Shimizu, I., Iwata, I., & Tanaka, M. 2014, MNRAS, 442, 1805
Inoue, A. K., Yamanaka, S., Ouchi, M., et al. 2020, PASJ, 72, 101
Itoh, R., Ouchi, M., Zhang, H., et al. 2018, ApJ, 867, 46
Jeeson-Daniel, A., Ciardi, B., Maio, U., et al. 2012, MNRAS, 424, 2193
Jiang, L., Egami, E., Fan, X., et al. 2013, ApJ, 773, 153
Kakiichi, K., & Dijkstra, M. 2018, MNRAS, 480, 5140
Kakuma, R., Ouchi, M., Harikane, Y., et al. 2021, ApJ, 916, 22
Kikuta, S., Matsuda, Y., Cen, R., et al. 2019, PASJ, 71, L2
Kollmeier, J. A., Zheng, Z., Davé, R., et al. 2010, ApJ, 708, 1048
Konno, A., Ouchi, M., Nakajima, K., et al. 2016, ApJ, 823, 20
Kovetz, E. D., Viero, M. P., Lidz, A., et al. 2017, arXiv:1709.09066
Kulkarni, G., Keating, L. C., Haehnelt, M. G., et al. 2019, MNRAS, 485, L24
Kusakabe, H., Shimasaku, K., Momose, R., et al. 2019, PASJ, 71, 55
Kusakabe, H., Shimasaku, K., Ouchi, M., et al. 2018, PASJ, 70, 4
Lake, E., Zheng, Z., Cen, R., et al. 2015, ApJ, 806, 46
Laursen, P., & Sommer-Larsen, J. 2007, ApJL, 657, L69
Laursen, P., Sommer-Larsen, J., & Razoumov, A. O. 2011, ApJ, 728, 52
Leclercq, F., Bacon, R., Verhamme, A., et al. 2020, A&A, 635, A82
Leclercq, F., Bacon, R., Wisotzki, L., et al. 2017, A&A, 608, A8
Li, T. Y., Wechsler, R. H., Devaraj, K., & Church, S. E. 2016, ApJ, 817, 169
Martin, D. C., Chang, D., Matuszewski, M., et al. 2014, ApJ, 786, 107
Mas-Ribas, L., & Dijkstra, M. 2016, ApJ, 822, 84
Mas-Ribas, L., Dijkstra, M., Hennawi, J. F., et al. 2017a, ApJ, 841, 19
Mas-Ribas, L., Hennawi, J. F., Dijkstra, M., et al. 2017b, ApJ, 846, 11
Matsuda, Y., Yamada, T., Hayashino, T., et al. 2012, MNRAS, 425, 878
Momose, R., Ouchi, M., Nakajima, K., et al. 2014, MNRAS, 442, 110
Momose, R., Ouchi, M., Nakajima, K., et al. 2016, MNRAS, 457, 2318
Momose, R., Shimasaku, K., Nagamine, K., et al. 2021a, ApJL, 912, L24
Momose, R., Shimizu, I., Nagamine, K., et al. 2021b, ApJ, 911, 98
Mukae, S., Ouchi, M., Cai, Z., et al. 2020, ApJ, 896, 45
Nakajima, K., Ouchi, M., Shimasaku, K., et al. 2012, ApJ, 745, 12
Navarro, J. F., Frenk, C. S., & White, S. D. M. 1997, ApJ, 490, 493
Oke, J. B., & Gunn, J. E. 1983, ApJ, 266, 713
Ono, Y., Itoh, R., Shibuya, T., et al. 2021, ApJ, 911, 78
Östlin, G., Hayes, M., Kunth, D., et al. 2009, AJ, 138, 923
Ouchi, M., Harikane, Y., Shibuya, T., et al. 2018, PASJ, 70, S13
Ouchi, M., Ono, Y., & Shibuya, T. 2020, ARA&A, 58, 617
Ouchi, M., Shimasaku, K., Furusawa, H., et al. 2010, ApJ, 723, 869
Péroux, C., & Howk, J. C. 2020, ARA&A, 58, 363
Pullen, A. R., Doré, O., & Bock, J. 2014, ApJ, 786, 111
Rauch, M., Haehnelt, M., Bunker, A., et al. 2008, ApJ, 681, 856
Rosdahl, J., & Blaizot, J. 2012, MNRAS, 423, 344
Scoville, N., Aussel, H., Brusa, M., et al. 2007, ApJS, 172, 1
Sekiguchi, K., Akiyama, M., Furusawa, H., et al. 2005, in Multiwavelength Mapping of Galaxy Formation and Evolution, ed. A. Renzini & R. Bender, Vol. 82 (Berlin: Springer), 82
Shibuya, T., Ouchi, M., Konno, A., et al. 2018, PASJ, 70, S14
Silva, M. B., Santos, M. G., Gong, Y., Cooray, A., & Bock, J. 2013, ApJ, 763, 132
Smith, A., Ma, X., Bromm, V., et al. 2019, MNRAS, 484, 39

Smith, A., Tsang, B. T. H., Bromm, V., & Milosavljević, M. 2018, MNRAS, 479, 2065
Steidel, C. C., Bogosavljević, M., Shapley, A. E., et al. 2011, ApJ, 736, 160
Steidel, C. C., Erb, D. K., Shapley, A. E., et al. 2010, ApJ, 717, 289
Swinbank, A. M., Bower, R. G., Smith, G. P., et al. 2007, MNRAS, 376, 479
Tanaka, M. 2015, ApJ, 801, 20
Tumlinson, J., Peeples, M. S., & Werk, J. K. 2017, ARA&A, 55, 389
Umehata, H., Fumagalli, M., Smail, I., et al. 2019, Sci, 366, 97
Verhamme, A., Dubois, Y., Blaizot, J., et al. 2012, A&A, 546, A111
Wisotzki, L., Bacon, R., Blaizot, J., et al. 2016, A&A, 587, A98
Wisotzki, L., Bacon, R., Brinchmann, J., et al. 2018, Natur, 562, 229
Wu, J., Jiang, L., & Ning, Y. 2020, ApJ, 891, 105
Xue, R., Lee, K.-S., Dey, A., et al. 2017, ApJ, 837, 172
Zhang, H., Ouchi, M., Itoh, R., et al. 2020, ApJ, 891, 177
Zheng, Z., Cen, R., Weinberg, D., Trac, H., & Miralda-Escudé, J. 2011, ApJ, 739, 62